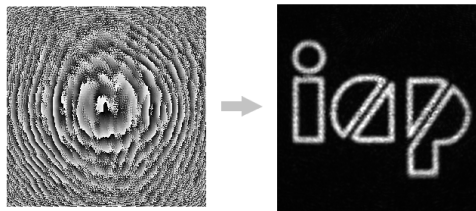# Robust Holographic Generation of Arbitrary Light Patterns: Method and Implementation

Masterarbeit in Physik

von

Weiqi Zhou-Hanf

angefertigt im
Institut für Angewandte Physik

vorgelegt der
Mathematisch-Naturwissenschaftlichen Fakultät
der
Rheinischen Friedrich-Wilhelms-Universität Bonn

Dezember 2018

I hereby declare that the work presented here was formulated by myself and that no sources or tools other than those cited were used.

Bonn, Dec 26th 2018

_____

Weiqi Zhou-Hanf

1. Gutachter

Prof. Dr. Dieter Meschede

2. Gutachter

Prof. Dr. Simon Stellmer

Blank Page.

Contents

Introduction

1.1 The phase problem and phase retrieval

In many scientific disciplines, the so called *phase problem* arises due to the fact that detectors can only measure the magnitude of diffracted waves and the phase of the signal of interest is missing, whereas the phase carries more the informations of a signal of interest than the magnitude does. This problem has a long history in X-ray crystallography [2, 3] and *phase retrieval* techniques have been developed to recover the phase information from unphased data - its Fourier magnitude. The most widely used method for phase retrieval are the *Gerchberg-Saxton algorithm* in 1972 [5] and its variants, for instance, the Gerchberg-Saxton-Misell algorithm in 1973 [6] and Fienup's hybrid input-output (HIO) algorithm in 1982 [9], which are still playing important roles in many fields today (2018), such as adaptive optics and radio astronomy [7, 8] and holographic imaging [27].

In the Discrete Quantum Simulator (DQSIM) experiment in Bonn, loosely called the quantum walk experiment in this thesis, it has been planned to study topologically protected transport of atoms along the edges separating distinct topological phases [10, 11]. To realize sharp edges, structured intensity patterns will be used and are to be holographically projected onto the caesium atoms trapped in a two-dimensional (2D) state-dependent optical lattice. A robust technique to reproduce sharp-edged diffracted patterns has been accomplished and is presented in this thesis. This technique is based on a Gerchberg-Saxton-like algorithm [23, 24], which has overcome the well-known stagnation problem and is able to suppress speckles induced by random phase vortices, and has further extended it to create sharp, diffraction-limited edges in the reconstructed intensity pattern. CGHs corresponding to the desired intensity patterns can be calculated with high computational efficiency (~ 100 iterations) and the intensity patterns can be reconstructed with high fidelity (relative RMS 3.9%).

1.2 Liquid crystal spatial light modulator

The pre-calculated holograms can be imprinted onto a traditional optical diffractive element (DOE) which is static. A more convenient hologram carrier is the digital and dynamic liquid crystal spatial light modulators (LC-SLMs), which are highly miniaturized active-matrix LC displays. The liquid crystals located in different pixel sites can alter the properties of incident light differently by changing their birefringence which is in turn controlled electrically [49, 50]. However, because of fabrication limitation, imperfections of SLMs are usually detected [35, 40, 41]. For phase-only modulation scheme, it's crucial to characterize the SLM beforehand, to make sure that the reflected wavefront from the SLM is not distorted by it and the phase response is gamma-corrected. A successful characterization of the utilized SLM is presented in this work. The measured reconstructed intensity patterns achieves a relative RMS of 7.6%, when the SLM compensation mask is applied.

1.3 Layout of this thesis

The work presented in this thesis consists of two main tasks. After a brief description of the relation between the phase retrieval problem and the quantum walk experiment (chapter 2), the first task aims to investigate the properties of the Gerchberg-Saxton algorithm in order to find a robust solution to the problem and to reconstruct desired intensity patterns reliably (chapter 3). After successful simulations and before the physical implementation, the second task is to characterize the SLM in order to compensate its physical and electrical phase errors before holographic applications (chapter 4). The experimentally reproduced intensity pattern are measured and compared with simulated ones (chapter 5). At the end, there will be a conclusion (chapter 6).

The phase problem

2.1 The origin of phase retrieval

The missing phase problem has to do with the fact that many times in the reality, detectors can only measure the magnitude of diffracted waves and cannot measure phase information. However, most of the information of a signal is carried by the phase, not by the magnitude. Given a signal of interest $f = A \cdot \exp(i\phi)$, the amplitude A contains the information of the energy of this signal and the phase $\phi = \phi_0 + kx + \omega t$ is carrying all the information about

- where it starts (ϕ_0),

- where it's going (kx), and

- how fast it gets there (ωt).

Phase retrieval is a century-old problem [1], having its origin in X-ray crystallography [2, 3]. X-ray crystallography is a method to determine the structure of a crystal. In such experiments, a collimated X-ray beam is stroke onto a crystal, the wave gets diffracted and a diffracted pattern is obtained. Since the wavelength of X-ray is so short, observers are almost immediately in the far field. Some physics (Appendix A.1.2) shows that the Fraunhofer diffraction is approximately the Fourier transform. Since the detector can only measure the magnitude of diffracted waves, what is measured is the (square) modulus of the Fourier transform of the signal of interest. A historically famous example is Gosling and Franklin's *Photo 51* [4], an X-ray diffraction image of crystallized DNA taken in the early 1950s, confirming the prior postulated double helical structure of DNA. In case of unknown structures that haven't been postulated, the phase retrieval problem remains an inverse problem: given that we only see the Fourier transform magnitude, how can we recover the phase?

2.2 Motivation based on the DQSIM experiment

The DQSIM project also pertains to the phase retrieval problem as well. In the 2D quantum walk experiment, topologically protected transport of the atoms state-dependently trapped in a 2D optical lattice has been theoretically analyzed and numerically simulated [10, 11] (Figure 2.1). The spatial boundaries between these distinct topological phases discussed in these works can be realized by imprinting structured intensity patterns onto the optical lattice, since the coin angle of the atom (or referred to as walker [10]) at a given lattice site is dependent on the intensity of the laser illuminating that site. The coin angle here describes the amount of a unitary rotation of the spin state into superposition of $|\uparrow\rangle$ and $|\downarrow\rangle$ and the coin operation is driven by microwave pulses [10], whose resonance can be modulated by a far-detuned laser based on the AC Stark effect. The ground state energy shift ΔE is linearly dependent of the laser intensity: $\Delta E \propto I/\delta$ [12]. δ is the detuning of the laser from the resonance of the involved transition.

A straightforward approach to create microscopic intensity patterns without mechanical change of the setup is holography. And because in the quantum walk experiment infrared laser is in use, whose wavelength is much larger than the wavelengths of X-ray (0.01 - 10 nm), the far-field distance would be of magnitude of 10 m. Therefore, a 2f-correlator (or 2f-system) is adopted to pull the far-field diffraction to the back focal plane of the Fourier lens, without loosing the Fourier transform property (Appendix A.1.3). In the control plane of the 2f-system, an SLM will imprint the pre-calculated hologram to the wavefront of the laser, such that the desired intensity pattern is later (~ 0.1 ns) reconstructed in the conjugate plane, namely the trapping plane.
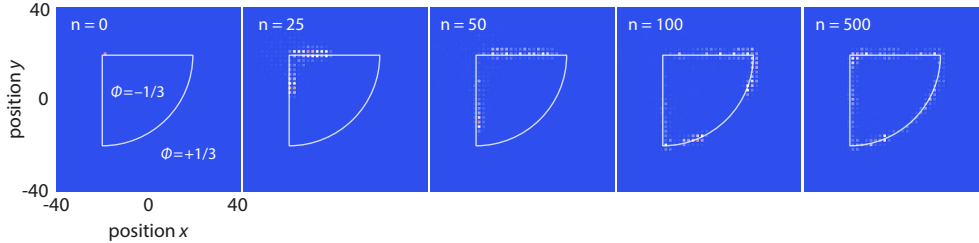

Fig. 2.1: Time evolution of the spatial probability distribution of a walker which is prepared in the lattice site close to the boundary of a quarter-circle-shaped topological island after n steps of walk [11].

For some well-known situations, the holograms can be obtained without effort, such as the Laguarre-Gaussian (LG) modes, also called doughnut modes informally. Those are known as the solutions of the wave equation in the cylindrical coordinates and are diffracted patterns of orbital angular momentum (OAM) beams which in turn can be induced by spiral phase plates (SPPs) at a circular aperture. The helical form that produces the OAM comes from the term $\exp(il\phi)$ [13], where $\phi \in [0, 2\pi]$ is the azimuthal phase and $l = 0, \pm 1, \pm 2, \ldots$ is referred to as the topological charge, counting the number of twists per wavelength. The essential feature in the diffracted doughnut modes is the centre of the patterns - the more twists per wavelength, the larger singularity of the beam, which in turn creates a bigger doughnut with a larger hole in the centre. If $l = 0$, the doughnut mode is reduced to an Airy disc. In practise, a blazed grating which is superimposed with the spiral phase is used in order to separate the first-order beam from the zeroth-order beam[1]. The linear superpostion of the spiral phase and the blazed grating is called fork grating, as its shape suggests. Fork gratings have the mathematical form

$$\phi_{\text{fork}}(x, y) = \text{mod } 2\pi[l \cdot arg(x + i \cdot y) + k \cdot x], \tag{2.1}$$

where k is the slope of the ramp. A set of simulations of SPPs, OAM wavefronts, fork gratings and LG$_{0l}$ modes for $l = 0, 1, 2, 3$ is shown in Figure 2.2. However, signal reconstruction from its Fourier magnitude, which is arbitrary, turns out to be non-trivial in general. For this, one needs to model the problem with more mathematical care.

---

[1] The zeroth-order beam is by definition the part of light that does not get modulated and can act as interfering background.
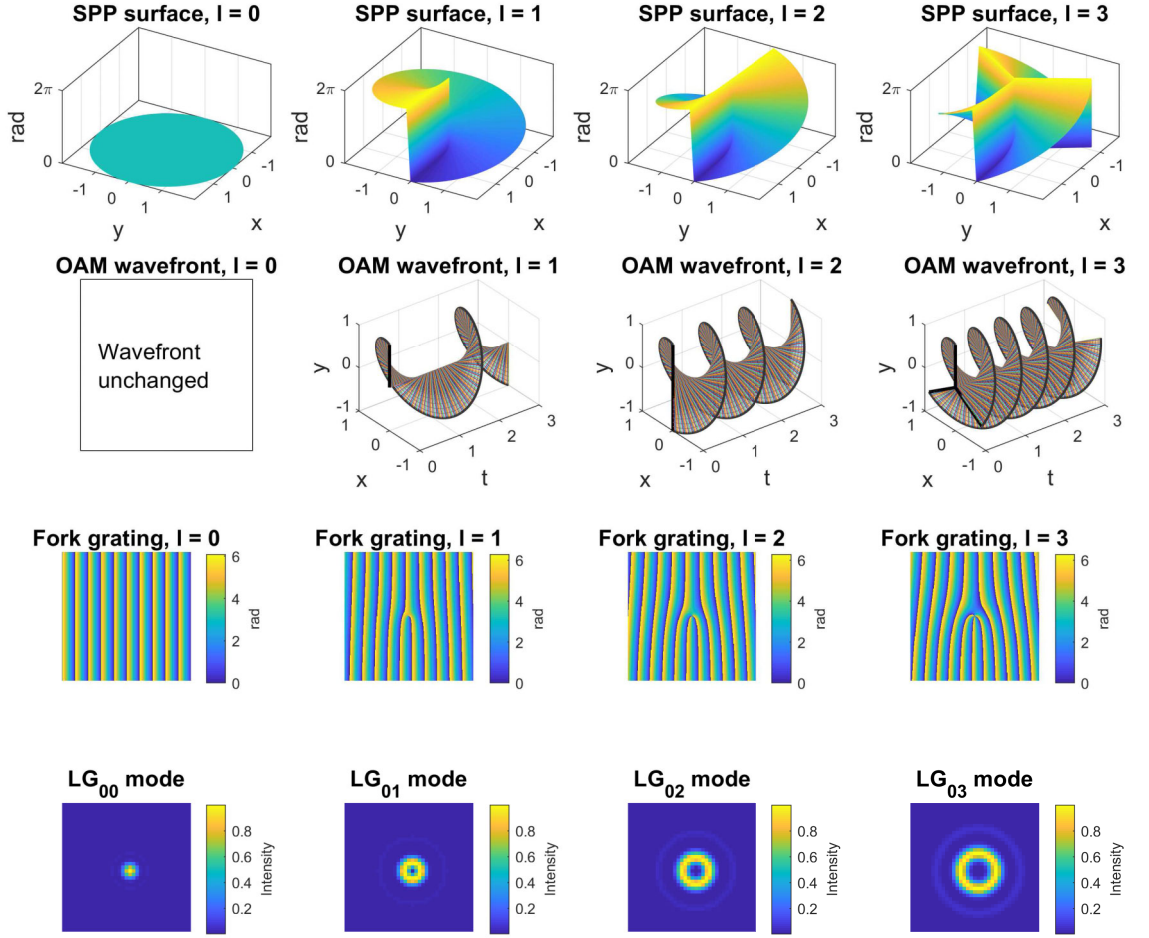
Fig. 2.2: Simulated spiral phase plates (the 1st row), OAM beam wavefronts (the 2nd row) and diffracted LG modes (the 4th row) with topological charge l = {0,1,2,3}. Closeup of the phase singularities of the blazed fork gratings is presented in the 3rd row. The incident beam is assumed to be flat with a uniform intensity.

2.3 Mathematical model

In general cases the phase retrieval problem cannot be solved analytically. It can be expressed as follow: given some real measurement $\boldsymbol{b}$, the Fourier (square) modulus constraint, find a complex $\boldsymbol{f}$ which is compatible with the equation

$$|\mathcal{F}\{\boldsymbol{f}\}|^2 = \boldsymbol{b}\,, \tag{2.2}$$

and consistent with some prior spatial modulus constraint, e.g. in X-ray crystallography one knows there is a bunch of atoms; in holographic projection one knows how the aperture should be. $\mathcal{F}$ denotes the Fourier transform. Equation 2.2 might look very simple, but in fact it describes a quadratic real non-holomorphic function with complex argument. Furthermore, at least one of the modulus constraints is non-convex (Section 3.1.2). Conventional optimization methods like gradient descent and error-reduction thus encounter feasibility problems. In complexity theory, the feasibility of solving this quadratic system exactly in polynomial time remains unclear and therefore, this problem remains NP-hard in general [31]. Herbert A. Hauptman and Jerome Karle have developed the direct method using the Sayre equation [14] for the determination of crystal structures and were awarded the Nobel Prize in Chemistry in 1985. The applications of their method were however limited, because the method is only suitable for small molecules and not for larger ones such as porteins [15]. A much more general and widely used method is a standard approach - the *Gerchberg-Saxton algorithm*, an iterative Fourier transform algorithm (IFTA) which has a wide range of applications beside crystallography. The structure, problems and extensions of this IFTA will be discussed about in detail in the following chapter.

Frameworks of phase retrieval

Since the phase retrieval problem turned out to be NP-hard, many heuristics have been developed to solve it. In microscopy and optics, the most-utilized method is the Gerchberg-Saxton (GS) algorithm, as already mentioned at the beginning. Sometimes it's also called *error-reduction algorithm* [9, 16, 34], because it does show a certain error-reduction property [16, 18]. It's also very often referred to as the *von Neumann's alternating projection* [16, 17, 33, 34] due to its algorithmic structure. The principle and the properties of the GS algorithm will be discussed in detail in sections 3.1.1 and 3.1.2.

This algorithm lacks a rigorous mathematical proof of the convergence [17, 33][1], but it works empirically well after several intuitive modifications and the intrinsic mechanism thereof is clear physically. This will be discussed and simulated in Section 3.1.3. Nevertheless, several further frameworks furnished with stronger mathematical background developed in applied mathematics and computer science as well as the benchmark problems will be conceptually reviewed in Section 3.2.

3.1 Projection-based framework

3.1.1 The principle of the GS algorithm

The GS algorithm is an iterative Fourier transform algorithm relying on linking the modulus in the object plane (specifically referred to as the SLM plane in this work) and observation plane by simulating light propagation back and forth between these planes. After each propagation, the prior modulus constraints in both planes, $A(x, y)$ and $T(u, v)$, are imposed to the resulted field. The phase freedom in the observation plane is completely released and the phase in the SLM plane is left to converge to the optimized solution $\phi(x, y)$. In another word, the GS algorithm aims to solve the equation

$$|\mathscr{F}\{A(x, y) \exp{(i\phi(x, y))}\}| = T(u, v) \tag{3.1}$$

iteratively as illustrated in Figure 3.1. This equation is equivalent to Equation 2.2, expressed in modulus. In this chapter, (x, y) and (u, v) denote coordinates in the SLM plane and observation plane, respectively.

---

[1] "Despite the widespread use of the algorithms proposed by these three researchers, current mathematical theory cannot explain their remarkable success." [17]. "It is in general completely unclear whether the Gerchberg-Saxton algorithm actually converges. (And if it were to converge, at what speed?) It is also unclear how the procedure should be initialized to yield accurate final estimates." [33].
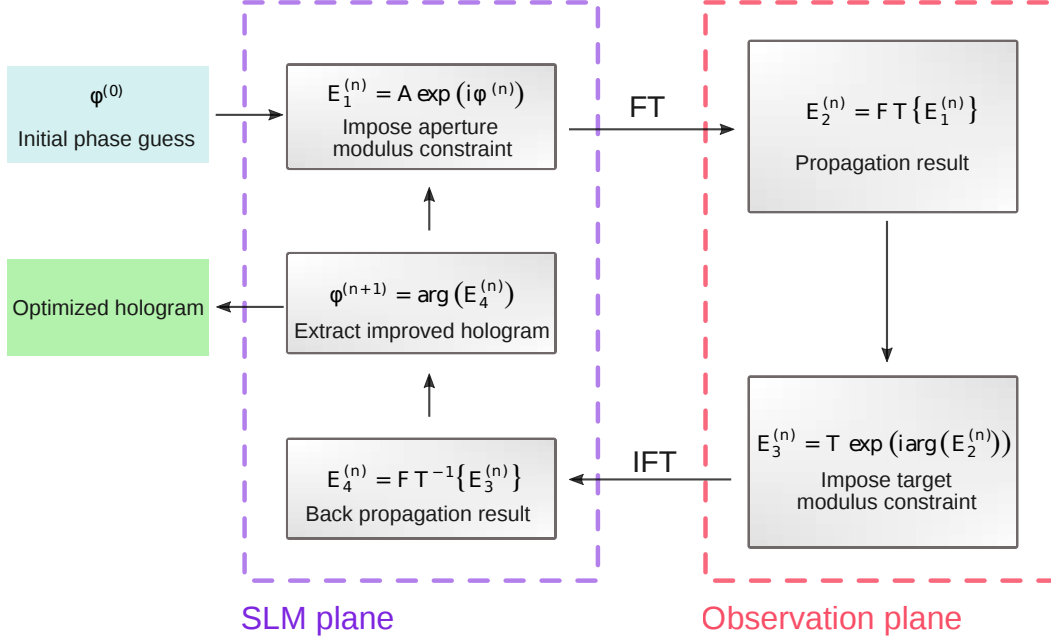
Fig. 3.1: Blockdiagram of the core Gerchberg-Saxton algorithm with explanatory notes of each step. The object plane (or spatial plane) is specified as the SLM plane. Starting from a random initial phase estimate, the algorithm loops between the SLM plane and the observation plane until the optimized hologram reproducing the desired intensity is obtained [24].

In the convex optimization, the error-reduction algorithm corresponds to the alternative projection, sometimes known as *projections onto convex sets* (POCS) [16, 17, 33, 34]. This insightful geometrical interpretation provides a posibility for understanding the fundamental idea behind the GS algorithm and gives a sound mathematical explanation of the stagnation problem. As suggested in [17], the GS algorithm can be reformulated in a general signal space, the complex Hilbert space

$$\mathscr{L} = L^2[\mathbb{R}^N, \mathbb{C}] . \tag{3.2}$$

The signal $\boldsymbol{f}(x) \in \mathbb{C}$ in Equation 2.2 in $\mathscr{L}$ is a square-integrable function of variable $x \in \mathbb{R}^N$. Then the spatial domain constraint is the set

$$C_1 = \{\boldsymbol{g} \in \mathscr{L} : \boldsymbol{g} \cdot 1_{A^c} = 0\} , \tag{3.3}$$

where $A \in \mathbb{R}^N$ is the support of the signal $\boldsymbol{f}$ (e.g. the aperture or the positions of atoms) and A^c the complement of A in $\mathbb{R}^N$ (e.g. area outside the aperture or area where there is no atom and the field should zero). 1_B denotes the characteristic function of the a set $B \in \mathbb{R}^N$. The Fourier modulus constraint is set

$$C_2 = \{\boldsymbol{g} \in \mathscr{L} : |\mathscr{F}\{\boldsymbol{g}\}| = T\} . \tag{3.4}$$

The phase retrieval problem is translated to the task of searching for a function $\boldsymbol{f} \in C_1 \cap C_2 \subset \mathscr{L}$, namely a point that satisfies both sets at the same time. Now let's associate a projection operator P_i ($i \in \{1, 2\}$) to each set C_i [16] and call $\boldsymbol{h} \in C_i$ the projection of $\boldsymbol{f}$ onto C_i if

$$||\boldsymbol{h} - \boldsymbol{f}|| = \min ||\boldsymbol{g} - \boldsymbol{f}||, \qquad \boldsymbol{g} \in C_i . \tag{3.5}$$

$|| \cdot ||$ denotes the norm. Therefore, the GS algorithm is now expressed in the following 4 steps:

1. Take an initial guess $\boldsymbol{f}_0 \in C_1$ of the signal of interest, whose phase is random

2. Project the guess onto set C_2 and create a new estimate $P_2 \boldsymbol{f}_n$,

3. Project the new estimate back onto set C_1 to make another guess $P_1 P_2 f_n$,

4. Let $f_{n+1} = P_1 P_2 f_n$. Repeat step 2 and step 3 and keep going until the pre-defined figure-of-merit function stops decreasing.

This algorithm is ad hoc. Sometimes it works and sometimes it doesn't. The outcome strongly depends on the initial guess. This is known as the stagnation problem [9]. Exploring the properties of the algorithm would help to understand this problem and lead to heuristic ideas for improvements.

3.1.2 Properties of the GS algorithm

A. The uniqueness of solution

Before describing the algorithm, it's appropriate to ask the question: is the solution to the problem described above uniquely defined? In other words, can a function be uniquely defined by its Fourier transform modulus? It has been shown that in 1D case a unique solution doesn't exist [2]. In contrast, the uniqueness[1] of 2D space exists under some conditions [19] and it is widely believed that 2D images generally fulfill the uniqueness conditions based on experimental results [16].

B. Non-convex property of the constraint set(s)

Definition. A set Ω is a convex set if the line segment joining any two points in Ω lies entirely in Ω. Algebraically, the set Ω is convex if $\forall f, g \in \Omega$ and $\forall \lambda \in [0, 1]$ [21]

$$\lambda f + (1 - \lambda)g \in \Omega. \tag{3.6}$$

It can be easily verified that the constraint set C_1 is convex and that C_2 is non-convex. The second statement is explicitly shown here. Choose an arbitrary $g \in C_2$. Then $-g \in C_2$ because $|-g| = |g|$, but $\frac{1}{2}g + \frac{1}{2}(-g) = 0 \notin C_2$.

C. Error-reduction property

The reduction[2] property of the error $e_n = ||g_n - g||$ (g is the desired image in Fourier domain and g_n the calculated one in nth iteration) was first investigated by Fienup in 1982 (Section II in [9]). Unfortunately, his notion was not strict and the proof turned out to be ambiguous. Levi and Stark established a connection between the GS algorithm and the non-convex POCS algorithm in 1984 (as discussed in Section 3.1.1) and have generalized the error-reduction property to the set-distance reduction property, where the distance between both constraint sets was involved, not the true error e_n (Section 2 in [16]). Osherovich also provided an intuitionistic proof of the set-distance reduction property in his PhD thesis (Chapter 3 in [18]), showing that the GS algorithm converges to a solution if the constraint sets are both convex. Because the set C_2 is non-convex, it's now very straightforward to understand the stagnation problem. This is visualized in Figure 3.2 with explanations in the caption.

D. Spontaneously generated optical vortices

Spontaneously generated optical vortices in the Fourier plane, often known as speckles, are induced by the random phase singularities in the spatial plane (SLM plane). Since the phase in such a singularity is indeterminate, the optical field there vanishes [22]. The topology of such vortices is similar as the doughnut modes introduced in Section 2.2. Every vortex of the speckle pattern also carries an optical angular momentum, but such vortices are undesirable. Their occurrence stalls the convergence of the GS algorithm, because they don't disappear automatically once being created; any fluctuation-induced zero-intensity-point during the iterations in turn serves as seed of the convergence-stalling

---

[1] We should note that the uniqueness of the function $f(x, y)$ is defined up to its trivial ambiguities such as $-f(x, y)$, $f(-x, -y)$, $f(x - x_0, y - y_0)$, which all have the same Fourier transform magnitude. [2] Reducing or at least nonincreasing.

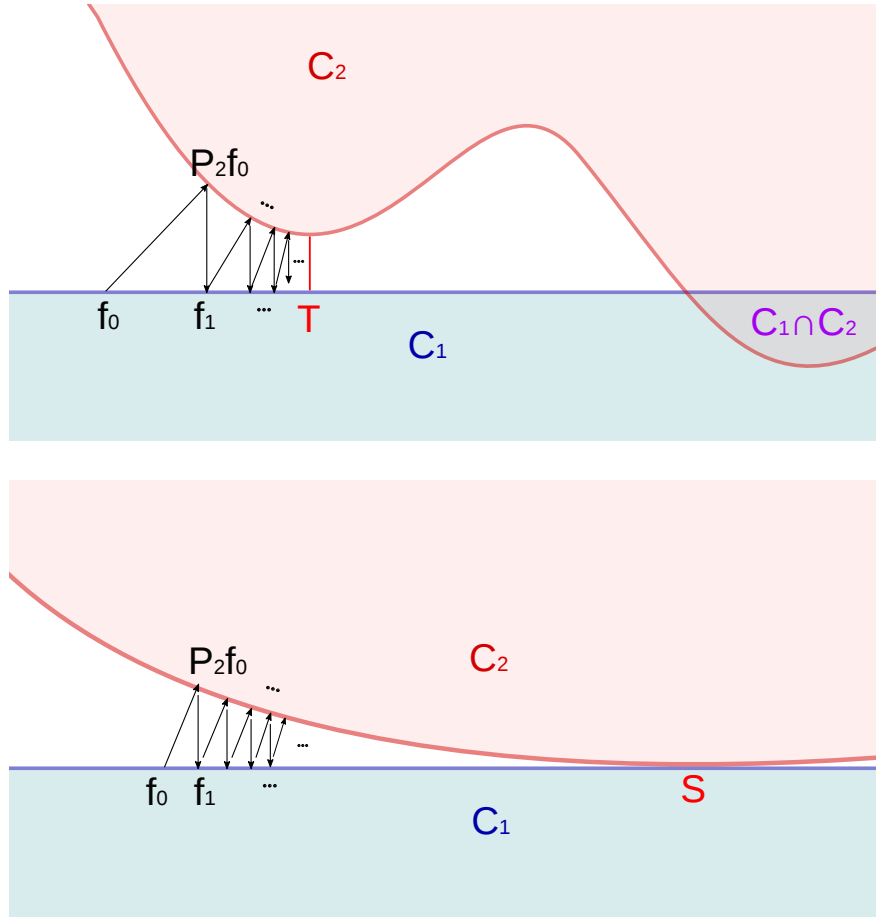vortices [24]. Therefore, measures must be taken in both conjugate planes to suppress the optical vortices [20].

Fig. 3.2: Alternating projections starting at point f_0. Upper: stagnation at T, whereas the true solution must be contained in $C_1 \cap C_2$ and this can only happen when non-convex set is involved. Lower: long tunnel toward the solution at S and this can occur to both convex and non-convex sets, leading to extremely slow convergence. These two sketches are redrawn from the convexity illustrations in [16].

3.1.3 SOMRAF algorithm: "3+1" empirical improvements

In the last four decades, many efforts have been made to solve the stagnation problem. For example, Fienup has proposed the hybrid input-output algorithm in 1982 [9], in which he treated f_n and f_{n+1} as the input and output of a non-linear system $P_1 P_2$ and relaxed the spatial domain constraint through a relaxation parameter - we will talk about the relaxation in a more general sense soon. Another crucial inspiration comes from Wyrowski and Bryngdahl's work in 1988 [20]. They verified that the random initial phase guess introduced many phase singularities and hence led to optical vortices in the Fourier plane. They suggested to use another initial phase guess and control the algorithm in a way that no new vortices are introduced during the iterative process. The ideas of the constraint relaxation, the alternative choice of initial phase guess and the control during the procedure are the important components of the method presented in this thesis, the *Softness-Offset-Mixed-Region-Amplitude-Freedom* (SOMRAF) algorithm. Bases on one or more of these pioneering inspirations, numerous variants of the GS algorithm have been developed and successfully implemented by physicists for their hologram calculation tasks specified by different scenes and requirements [23, 24, 25, 26, 27]. In the upcoming content, the SOMRAF algorithm will be described in four steps, followed by detailed numerical simulations of two test patterns.

Step 1: relaxation of the modulus constraint

In [16], the projectors associated to both constraint sets have been generalized to the relaxed versions

$$P_i \rightarrow K_i = (1 - \mu_i) \cdot \mathbb{1} + \mu_i \cdot P_i, \qquad i = \{1, 2\}, \tag{3.7}$$

by introducing the relaxation parameters μ_i which lie between 0 and 1. Fienup's hybrid-input-output (HIO) algorithm [9] relaxes the projector to the spatial domain constraint C_1 and thus has the form [16]

$$\boldsymbol{f}_{n+1} = P_2 K_1 \boldsymbol{f}_n. \tag{3.8}$$

In another category, the operator to the Fourier domain constraint C_2 is relaxed, namely

$$\boldsymbol{f}_{n+1} = P_1 K_2 \boldsymbol{f}_n, \tag{3.9}$$

the representing algorithm of which is the adaptive-additive (AA) algorithm [28]. In the AA algorithm, $E_3^{(n)}$ in Figure 3.1 becomes

$$E_3^{(n)} = \left[\mu \cdot T + (1 - \mu) \cdot \mid E_2^{(n)} \mid \right] \mathrm{e}^{i \arg(E_2^{(n)})}, \tag{3.10}$$

and this is the starting point of the SOMRAF algorithm which is an extension of the Mixed-Region-Amplitude-Freedom (MRAF) algorithm [23] and the Offset-Mixed-Region-Amplitude-Freedom (OM-RAF) algorithm [24]. In contrast with the AA algorithm which introduces the amplitude freedom uniformly to the Fourier domain, the MRAF algorithm separates the Fourier plane into subsets, a small area around the desired pattern named signal region (SR) and its complement called the noise region (NR). In the SR the modulus constraint is completely maintained and in the NR the amplitude freedom is totally released. Equation 3.10 thus becomes

$$E_3^{(n)} = \left[\mu \cdot T \mid_{SR} + (1 - \mu) \cdot \mid E_2^{(n)} \mid_{NR} \right] \mathrm{e}^{i \arg(E_2^{(n)})} \tag{3.11}$$

in the MRAF algorithm. The result is that the algorithm converges in the SR very closely to the target pattern and what happens in the NR causes less concern, because in the atom confinement experiments there will be no atom in this region. This step forces the algorithm to concentrate only in the SR. However, amplitude freedom relaxation alone is not sufficient to reproduce the desired intensity pattern without suffering speckles. The next two steps are also crucial for speckles suppression.

Step 2: quadratic initial phase guess

The underlying physics of optical vortices has been discussed. One idea in [20] is to replace the random initial phase guess by a more appropriate one, such that no intensity zero is produced at the very beginning. The MRAF algorithm proposes to apply a quadratic initial phase guess, which already produces a result close to the target pattern in the first iteration. In this scene, the new initial guess not only suppresses phase vortices, but also starts at a position close to the global optimum in the SR.

Step 3: finite intensity offset in the Fourier domain

The second measure to suppress phase vortices is to avoid their seed - zero intensity point created during the iterative procedure due to fluctuations. For this, the OMRAF algorithm simply offsets the target intensity by a uniform and finite amount Δ^2 [24]. This step redefines the zero of the intensity to which all intensity values are referenced, but the physics remains the same. Hence, the target amplitude becomes

$$T \rightarrow \sqrt{T^2 + \Delta^2}. \tag{3.12}$$

Step 4: softness for sharp edges

For target with sharp edges, the OMRAF algorithm is not yet sufficient to reproduce high-accuracy patterns that are required for the quantum walk experiment. Fringing artefacts which apparently look like the knife-edge effect of Fresnel diffraction (Appendix A.1.1) occur when the OMRAF algorithm is applied to reconstruct sharp-edged intensities. An empirical idea to suppress these fringing artefacts is to introduce a tunable softness to the target pattern. The softness is obtained by convolving the desired sharp-edged target pattern with a Gaussian kernel whose width is used to control the softness. During the iterations, the softness can be reduced gradually to end up with the sharp edges.

Numerical simulations using MATLAB

For evaluation of the performance of the SOMRAF algorithm, two test patterns related the experiment [11] have been chosen. For the sake of simplicity, the algorithm is demonstrated with the first test pattern "**plateau**", the boundary of which is a quarter of a circle with a radius of 30 Fourier pixels[1]. This binary-valued pattern is convenient for evaluating the achieved relative RMS and the signal-to-noise ratio (SNR). To investigate the resolution of the algorithm and the experiment, a second test pattern "**ramps**" will be used, the details of which will be described at the last of this subsection.

The matrix of the hologram is chosen to be 700×700 pixels.[2] Let the physical size of the matrix side length be d, then the Fourier pixel has a physical size of $\lambda f/d$, with $\lambda = 852$ nm the wavelength and $f = 150$ mm the focal length of the Fourier lens chosen for the holography experiment. The calculated hologram will be transferred to an LCoS SLM with pixel pitch of 10.4 μm and thus the Fourier pixel is 17.6 μm physically. In order that the discrete Fourier transform can resolve the output plane and calculate the CGH in the input plane, the hologram matrix is embedded at the centre of a 1400×1400 zero matrix, known as zero-padding and required by the Nyquist sampling theorem. The subsets NR and SR of the output plane introduced by the MRAF algorithm [23] are visualized in Figure 3.3, based on the reconstructed pattern "plateau" in zoom-in view. The desired 30×30 Fourier pixels pattern lies in the measure region (MR), surrounded by the red square; the signal region, selected to be 105×105 Fourier pixels, is surrounded by the yellow square and includes the signal region. The target amplitude is now imprinted in SR. The area outside the yellow square is the noise region, where the phase and amplitude freedom are totally allowed.
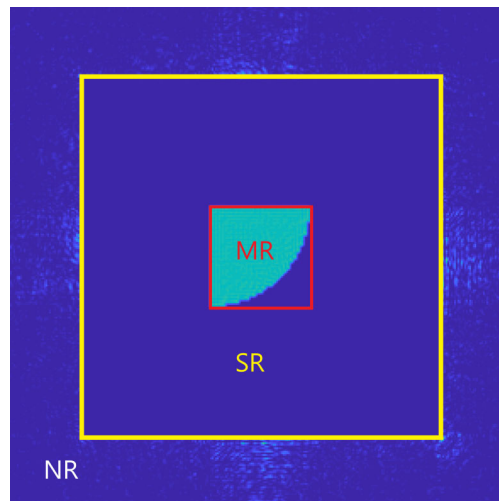

Fig. 3.3: Visualization of the noise region (NR), signal region (SR) and measure region (MR) based on the (zoom-in) reconstructed intensity pattern "plateau" using the SOMRAF algorithm.

---

[1] In this thesis, the Fourier pixel is defined as the pixel of the output plane (Fourier domain), i.e. the resolution unit of the algorithm. [2] Pixel of the input plane, in the implementation in Chapter 4 this corresponds to the SLM physical pixel pitch.

The quadratic initial phase, which should produce diffracted pattern in a similar scale as the desired one, has the form

$$\phi_Q = q \cdot (x^2 + y^2), \tag{3.13}$$

with a single parameter q controlling the size of the diffracted pattern in the first iteration. For the pattern "plateau", the optimal value of q is $0.22\,\text{mrad/pixel}^2$, manually[1] determined by observing the behaviour of the figure-of-merit function and the quality of the reconstructed intensity pattern for a wide range of values. This is the principle of optimizing all parameters mentioned below. As also observed in [23], it's found that small change in q didn't affect the final result. Comparisons of the random initial phase guess and quadratic initial phase guess as well as the corresponding results are shown in the Figure 3.4. In the OMRAF algorithm [24], the optimized offset Δ^2 was $\sim 1\%$ of the maximal intensity in the trapping plane and was only needed in the first iteration. The author believed that very few vortices would be formed in the following iterations. In the SOMRAF algorithm, Δ^2 is optimized to 0.5% of the maximal intensity in the signal region and has to be maintained for every iteration. The the optimized value of the relaxation parameter μ is found to be 0.4, in agreement with the result of [24][2]. The width of a normalized Gaussian kernel that controls the softness of the sharp-edged pattern is optimized to 0.5 pixel.
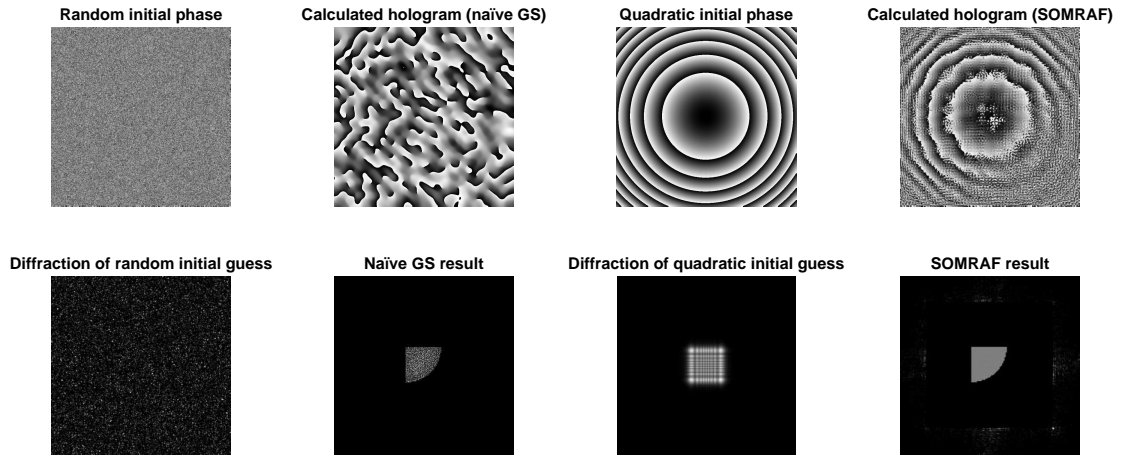
Fig. 3.4: Initial phase guesses and the reconstructed intensities of the naïve Gerchberg-Saxton algorithm and the SOMRAF algorithm. The first column is the random initial phase guess and its diffraction; the second column is the calculated result of the GS algorithm; the third and the fourth columns are the situation of the SOMRAF algorithm. In the GS case, the calculated hologram contains numerous phase singularities and the reconstructed intensity is consequently full of speckles despite the correct shape. In the SOMRAF case, no optical vortex is found.

To gauge the performance of the SOMRAF algorithm and to optimize the parameters mentioned above, a figure-of-merit function which visualizes the convergence of a algorithm is defined in the output plane:

$$\eta = \frac{1}{N_{\text{MR}}} \cdot \frac{||\tilde{I}_n(u,v) - \tilde{I}_0(u,v)||}{||\tilde{I}_0(u,v)||}, \qquad (u,v) \in \text{MR}. \tag{3.14}$$

In Equation 3.14, $\tilde{I}_n = I_n / \sum_{(u,v) \in \text{MR}} I_n$ is the reconstructed intensity in the nth iteration and $\tilde{I}_0 = I_0 / \sum_{(u,v) \in \text{MR}} I_0$ the target intenstiy, both normalized to have the same power in the MR. N_{MR} is

---

[1] In some very informal occasions, (funny) people called manual parameter optimizations the "GSS algorithm", the full name of which is Graduate Student Search algorithm. In principle, one can define proper functions that automatically optimize the parameters. However, the complexity usually increases exponentially with increasing dimensions of the problem. Manual optimizations are more practical and preferred due to time constraint.   [2] Gaunt has documented the result $\mu = 0.4$ in another unpublished article in 2011, *Coherent Optical Sculpting for Manipulating and Probing Ultracold Atoms.*

the number of Fourier pixels in MR. Before discussing about the relative RMS and the SNR of the reconstructed intensity pattern, the signal area and the background noise area[1] are defined as the plateau area (inside the quarter of circle) and its complement in the MR, respectively. The definitions of RMS and SNR are

$$\text{RMS}(\%) = \frac{rms(Signal - mean(Signal))}{mean(Signal)}, \tag{3.15}$$

$$\text{SNR}(\text{dB}) = 10 \cdot \log_{10} \frac{mean(Signal) - mean(Background)}{rms(Background - mean(Background))}. \tag{3.16}$$

The light usage efficiency (LUE), defined as the ratio of the intensity in the signal region to the total intensity in the output plane, also causes attention. The LUE in the GS algorithm is supposed to be 100% and in the relaxed versions much less, depending on the value of parameter μ. Now the performances of the SOMRAF algorithm can be compared to the OMRAF algorithm and the naïve GS algorithm in different perspectives. The parameters q for the initial phase guess and Δ^2 for the intensity offset are set the same for the OMRAF algorithm and the SOMRAF algorithm. The comparison of algorithm convergence is shown in Figure 3.5 in two types of axis scaling. The reconstructed intensities are compared with the desired one in 2D (Figure 3.6) and 3D (Figure 3.7). The relative RMS, SNR and LUE of three algorithms are summarized in table 3.1. The calculated holograms can be found in Appendix A.2.1.

Figure 3.5 shows that the GS algorithm is trapped in some local minimum after 25 iterations, while the OMRAF algorithm has made a much larger drop already after 25 iterations. But the merit function of the OMRAF algorithm is apparently not monotonically decreasing in this case. The SOMRAF algorithm has enabled a further drop and keeps dropping, as it can be seen in the natural logarithmic scaling plot. However, it seems that the SOMRAF algorithm has reached a tunnel that has been discussed before (Figure 3.2). In figures 3.6 and 3.7, the speckle problem is very well visualized in the intensity reconstructed by the GS algorithm. The OMRAF algorithm has solved the speckle problem, but the edge behaviour in the reconstructed intensity is undesirable. After the softness is introduced, the SOMRAF algorithm can finally reproduce intensity pattern that is very close to the desired one. Since the Fourier domain amplitude freedom is partially released in the OMRAF algorithm and the SOMRAF algorithm, light is allowed to be diffracted into the noise region without further care and hence the LUE has dropped by a factor of 1/2. A correlation between the relaxation parameter μ and the achieved LUE was not established though. Too large or too small μ led to speckles again. Although the OMRAF algorithm has appreciably reduced the flatness RMS from the GS result 53% to 13%, the SOMRAF algorithm further brings it down to a level of few percent. Besides, the enhancement (of a factor of 9) in SNR is large comparing to the GS and OMRAF algorithm.

	Naïve GS	OMRAF	SOMRAF
LUE	99%	43%	45%
RMS	53%	13%	3.9%
SNR	13.1 dB	13.2 dB	22.5 dB

Tab. 3.1: Summary of reconstructed pattern "plateau".

---

[1] Not the signal region and noise region defined in the algorithm structure.
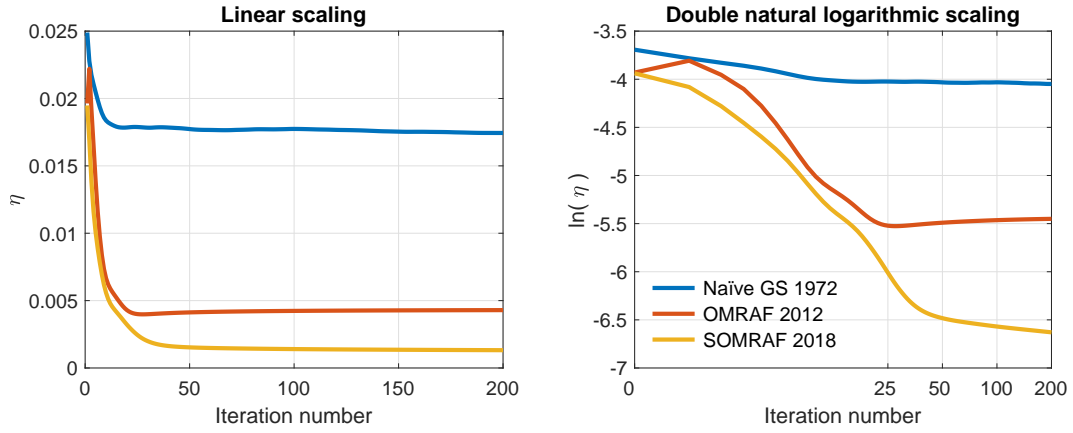
Fig. 3.5: Comparison of the figure-of-merit functions of reconstructing the pattern "plateau".
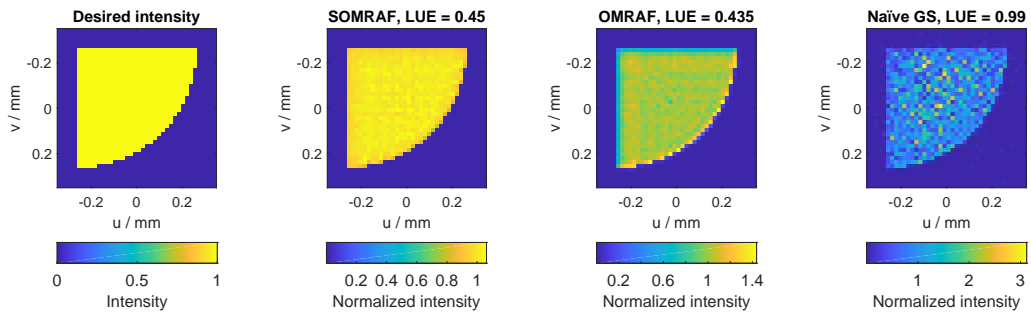

Fig. 3.6: 2D visual comparison of the reconstructed intensities of pattern "plateau". The axes are rescaled to the physical size in the output plane.
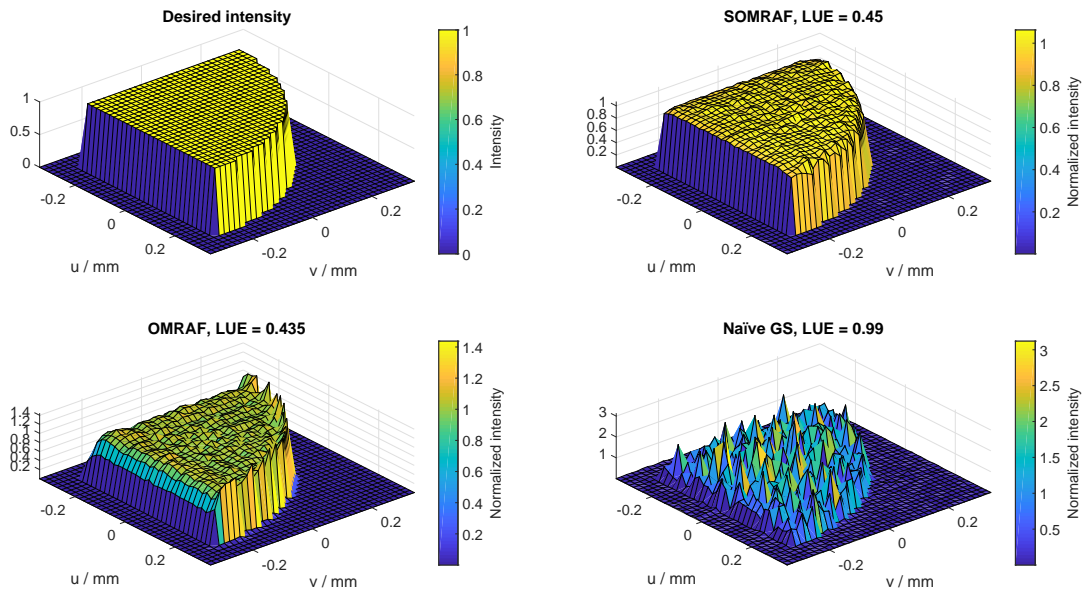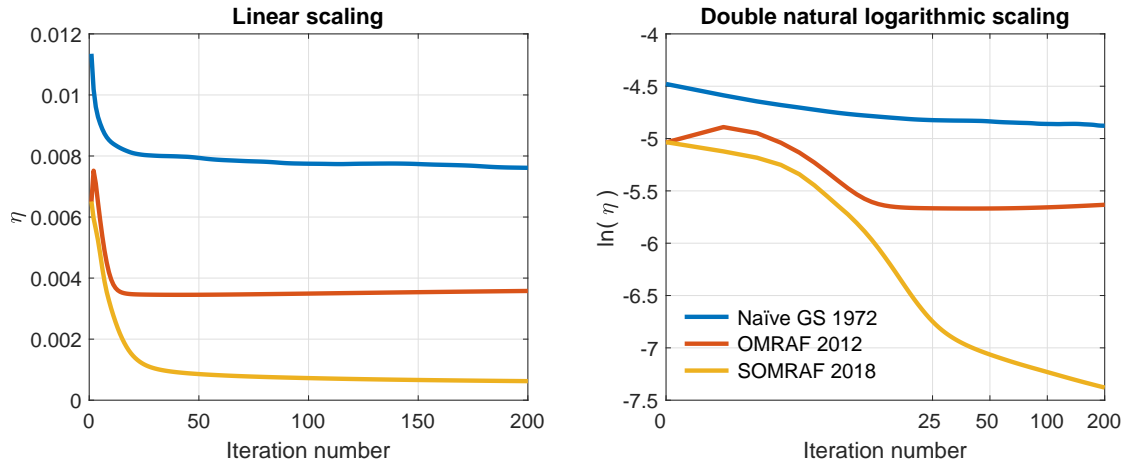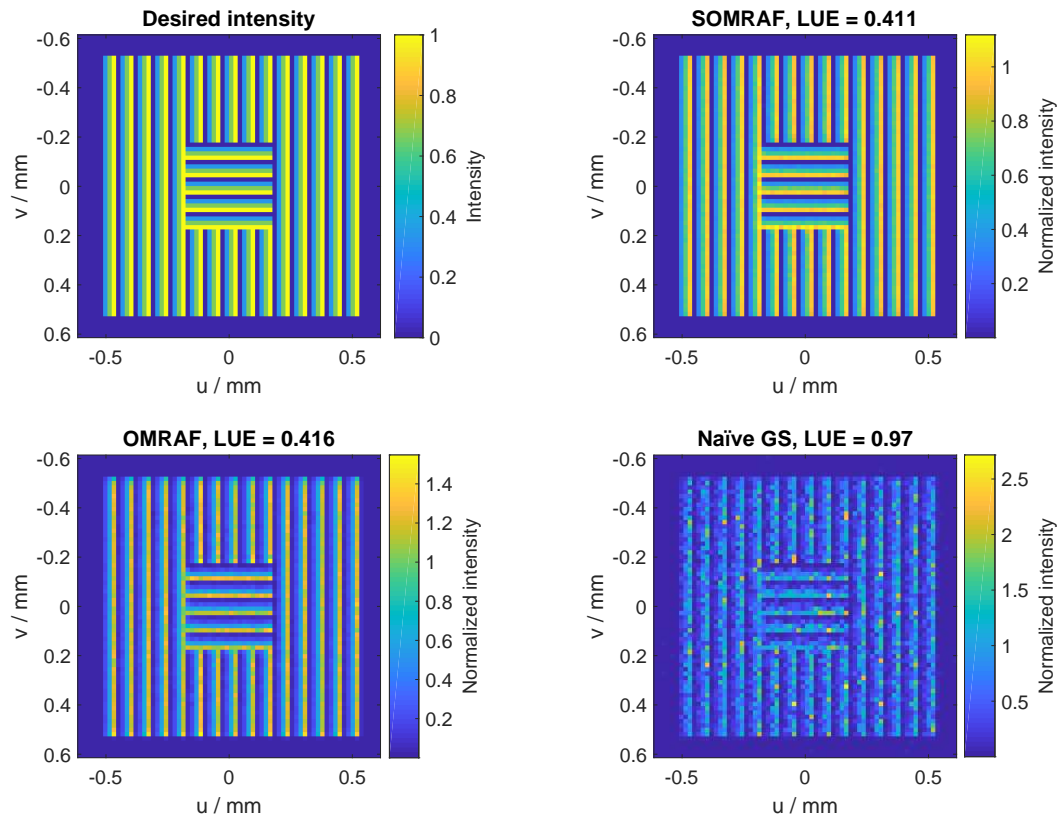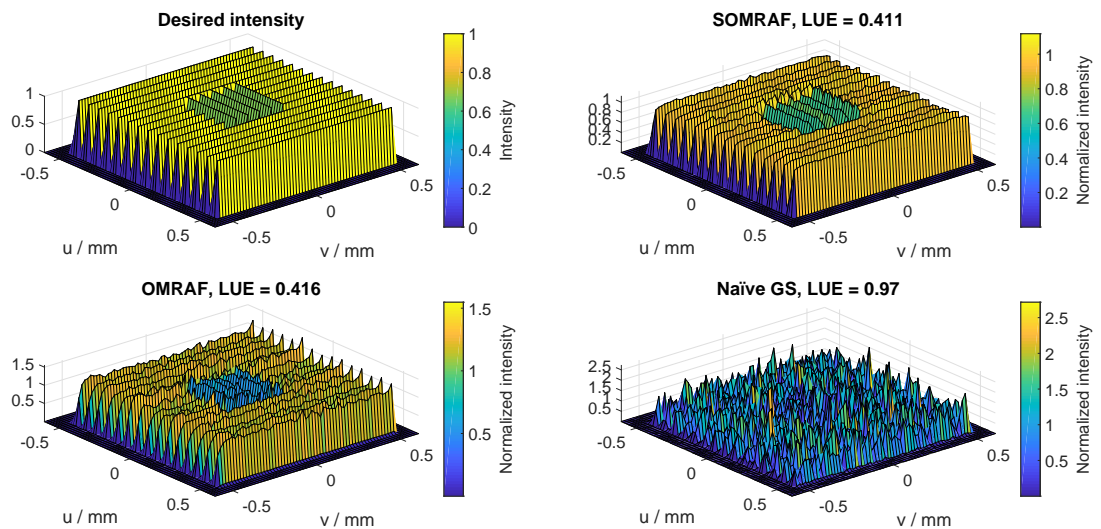

Fig. 3.7: 3D visual comparison of the reconstructed intensities of pattern "plateau". The axes are rescaled to the physical size in the output plane. All reconstructed intensities have been normalized to the power of the desired intensity.

To examine resolution that the physical implementation can achieve (next chapter), the second test

pattern "**ramps**" is employed, which consists of two concentric squares with linear discrete ramps inside each. The direction of ramps in the outer area is perpendicular to the ramps direction in the inner square. Each ramp has 4 Fourier pixels. In the quantum walk experiment, an intensity raster will be imprinted onto the atoms trapped in the optical lattice, 3 atoms (i.e. 3 lattice sites) per ramp (Figure 3.8) [11]. The grating constant of the lattice site is 612 µm and the Abbe radius of the imaging system is 463 µm according to Abbe's resolution criterion $r_{Abbe} = 1/(2\text{NA})$, where the numerical aperture (NA) of the objective is 0.92 [29, 30]. In this scene, 4 Abbe radii will be projected onto each ramp. To simulate this, 4 Fourier pixels (resolution unit of the Fourier transform, later implemented by a physical lens) is put into each ramp. Entirely, the pattern "ramps" has 60×60 Fourier pixels. The 20×20 pixels inner square contain 5 vertical ramps and the outer area has 15 horizontal ramps. This pattern is also reconstructed by the GS, OMRAF and SOMRAF algorithms. Results are shown in figures 3.9 to 3.11 and the corresponding holograms can also be found in Appendix A.2.1.
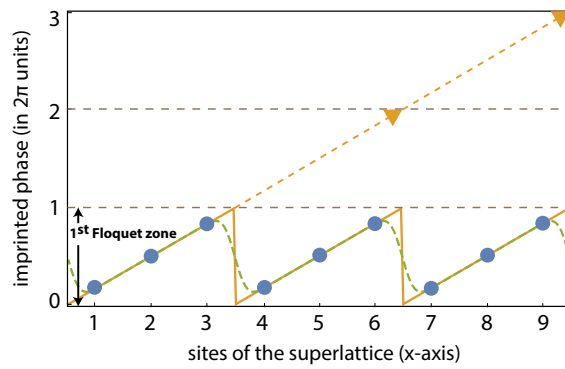
Fig. 3.8: Sideview of three ramps of the desired intensity pattern "ramps" [11].

Fig. 3.9: Comparison of the figure-of-merit functions of reconstructing the pattern "ramps".

Fig. 3.10: 2D visual comparison of the reconstructed intensities of pattern "ramps". The axes are rescaled to the physical size in the output plane.

Fig. 3.11: 3D visual comparison of the reconstructed intensities of pattern "ramps". The axes are rescaled to the physical size in the output plane. All reconstructed intensities have been normalized to the power of the desired intensity.

The convergences of the three algorithms (Figure 3.9) show very similar behaviours as in the first case "plateau". The extremity of this test pattern is that along the corresponding ramps direction, adjacent Fourier pixels are associated with distinct values. Therefore this pattern can be used to examine the

17

resolution of the algorithms. The GS result in Figure 3.10 and 3.11 turns out to be totally noisy, as it was also the case for the other pattern. The OMRAF result can associate roughly the desired values to the Fourier pixels, but the quality of the reconstructed pattern suffers from the edge problem. The SOMRAF algorithm is able to reconstruct the desired pattern very close to the target. For a further visual comparison, the 15 outer ramps in two selected regions (Fourier pixel 1 - 20 and 41 - 60 along the v-axis) are averaged and the 1D profiles of the three algorithms are compared to the target, see Figure 3.12.
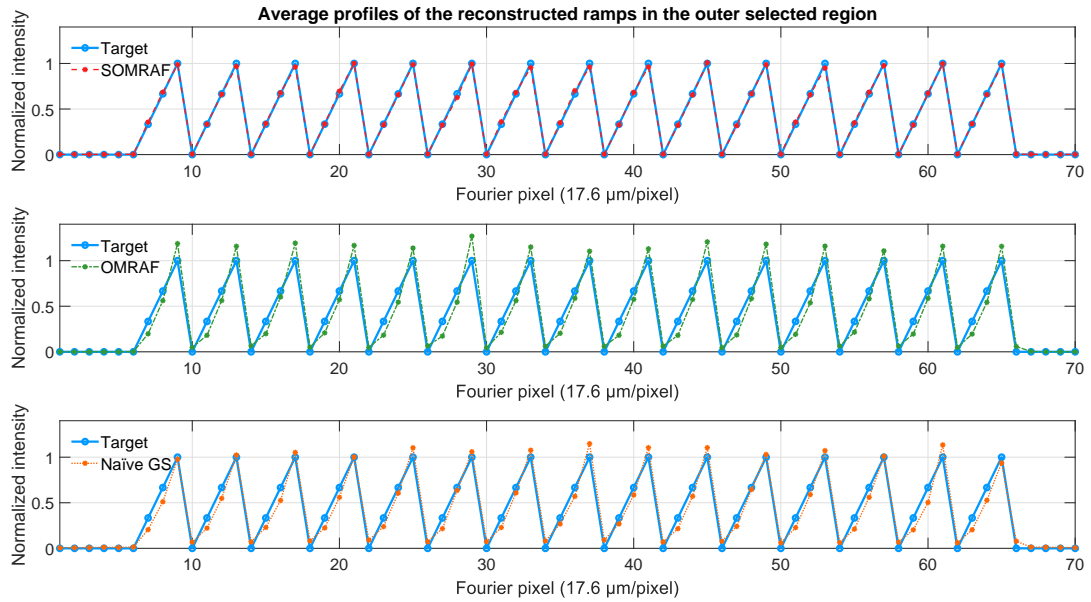
Fig. 3.12: Comparison of the reconstructed average profiles of the selected ramps. The SOMRAF result (the 1st plot) is very close to the target and the desired sharp edges are numerically very well realized, while the OMRAF result (the 2nd plot) and the GS result (the 3rd plot) show obvious deviations from the target profile.

3.2 Other frameworks and benchmark problems

In the recent decade, scientists working in the fields of applied mathematics and computer science have also developed various frameworks and algorithms to solve the phase retrieval problem. Remarkable works are done by Emmanuel Candès from Stanford University, who worked with the Fields medal winner Terence Tao in 2006 in *Compressed Sensing* that allows the recovery of objects with a below-Nyquist sampling rate. Two frameworks for phase retrieval suggested by Candès and his collaborators are conceptually reviewed in this section.

3.2.1 Convex optimization and gradient method

In the foregoing section, the non-convex property of the phase retrieval problem has already been discussed and under this context, convex optimization encounters feasibility problem. However, the *PhaseLift* technique [31] suggests to treat the (non-)convexity of optimization as a coordinate-dependent problem. The phase retrieval problem can be reformulated as a rank-one minimization problem, which is relaxed by a convex trace norm minimization [31]. Another similar convex re-laxation *PhaseCut* [32] suggests to split the phase and magnitude via a complex semi-definite pro-gramming. Applying conventional gradient methods like gradient descent or Newton's method on the phase retrieval problem also encounters feasibility problem. That is, a real function of complex arguement z is not holomorphic (i.e. not complex-differentiable) unless it is constant. This can be easily proven by the Cauchy-Riemann equations. And this is exactly the situation of Equation 2.2. Therefore one needs to re-define the gradient and Hessian in order to use the gradient method for the phase problem. The Wirtinger calculus provides such possibilities: $f(z)$ is not holomorphic at z, but $f(z, \bar{z})$ is holomorphic at z for a fixed $\bar{z}$, and vice versa. $\bar{z}$ is the complex conjugate of z. This is the essence of the *Wirtinger Flow* algorithm [33] for exact phase retrieval.

3.2.2 Benchmark problems
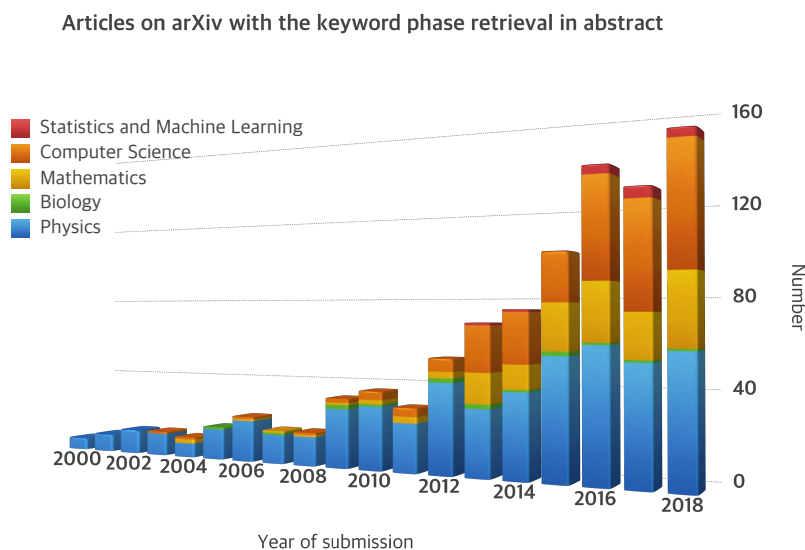
Fig. 3.13: Mathematical and numerical aspects of the phase retrieval problem have received considerable atten-tions since 2011. Source: arXiv databank, November 2018.

These two frameworks have encouraged a wide range of mathematical and algorithmic approaches of the phase recovery task. A rough count of arXiv articles with the keyword "phase retrieval" in abstract has shown this trend (Figure 3.13). Veit Elser, professor of physics at Cornell University, has noticed

this trend and brought up the benchmark problems for evaluating the performance of algorithms [34] and he also strongly suggested to solve the phase problem on the basis of fundamental physics rather than pure mathematics. However, his proposal is based on crystallography in particular, where the two constraint sets look different from those in holography (sets C_1 and C_2 discussed in the Section 3.1.1 and 3.1.2). For atom confinement experiments, I haven't found another competitive algorithm that has been able to reconstruct high-fidelity and high-SNR intensity pattern efficiently as the MRAF-OMRAF-SOMRAF branch in the family of GS-like algorithms. In addition, the SOMRAF algorithm has a succinct structure whose mechanism is physically clear.

Physical implementation: spatial light modulator

The phase change of a wave depends on the optical path length nd, with n the index of refraction and d the thickness of the medium that the wave passes through. Static diffractive optical elements (DOE) such as phase plates with spatially varying thickness can serve as the carriers of the holograms. In contrast to the human intervention during the acquisition stage of the phase plates, digital spatial light modulators (SLMs) show increased flexibility and user friendliness, especially when dynamic altering of the hologram is required during the experiment.

4.1 Introduction of SLMs

4.1.1 Construction of LCoS PAN and operation principle

A 10-bit 1050×1440 pixels Liquid Crystal on Silicon (LCoS) SLM in parallelly aligned nematic (PAN) configuration from the company Santec is used in this experiment, operating for the 852 nm laser. LCoS SLM is often called LC-SLM, which is a highly miniaturized (Santec SLM-100: pixel size 10 μm, pixel pitch 10.4 μm) reflective active-matrix LC display. The principle of the phase modulation is to alter the index of refraction seen by the extra-ordinary beam passing through the electrically controlled birefringent LC material sandwiched between the transparent electrode and the pixelated reflecting electrodes. Therefore, to obtain an optimal performance for the phase-only modulation, the polarization of the incident light should coincide with the optical axis of the LCoS in PAN configuration, see Figure 4.1f.
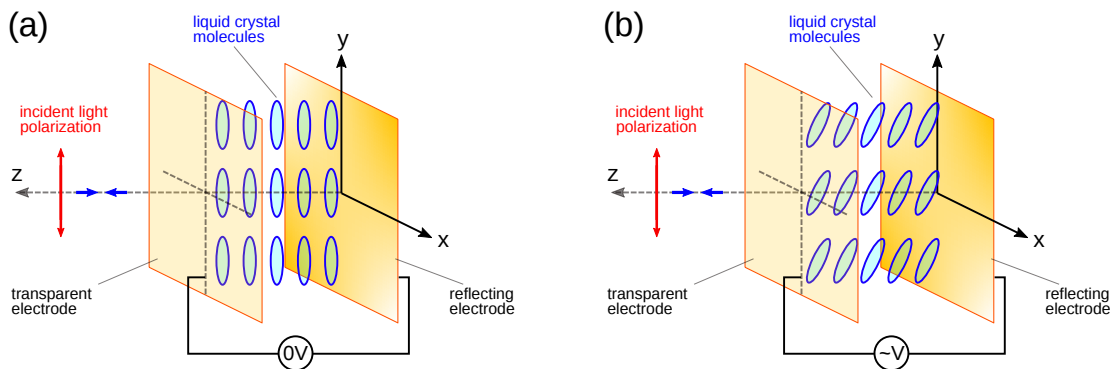
Fig. 4.1: Illustrations of PAN configuration with (a) OFF voltage and (b) ON voltage states.

The modulated phase of an LCoS device is give by

$$\Delta\phi = \frac{2\pi(2d)\Delta n}{\lambda},$$ (4.1)

where d is the LC layer thickness and $\Delta n = n_{\text{eff}} - n_o$ the birefringence at wavelength λ [49, 50]. The effective refractive index n_{eff} and hence the phase for each pixel can be altered ($n_o < n_{\text{eff}} < n_e$) by rotating the rod-shaped LC molecules. This is achieved by controlling the electric field over the pixel, i.e. applying a voltage over the pixel electrode and the common electrode, see Figure 4.1 and Figure 4.3. The SLM is addressed with a 10-bit number, referred to as the grayscale level, which is converted into voltage by the SLM driving hardware. In the ideal case, where no physical or electrical error is present, the modulated phase is proportional to the grayscale level and the applied voltage uniformly in the entire matrix. One advantage of reflective type LC-SLM can easily be seen in Equation 4.1 - light passes twice through the LC layer and hence increases the modulation range. By choosing incident polarization along the LC director axis, it's able to realize pure phase-only modulation without influencing the polarization and the amplitude.

In addition to phase-only modulation, PAN configuration also allows polarization modulation, when the component orthogonal to the SLM optical axis is present (see $|\uparrow\rangle$ below):

$$|\psi\rangle = \alpha \, |\uparrow\rangle + \beta \, |\rightarrow\rangle \quad \Rightarrow \quad |\psi'\rangle = \alpha \, |\uparrow\rangle + \mathrm{e}^{i\Delta\phi}\beta \, |\rightarrow\rangle \,.$$

Consequently, amplitude/intensity modulation can also be realized:

$$I \propto | \langle\psi|\psi'\rangle |^2 \propto \cos(\Delta\phi)\,.$$

4.1.2 The effect of spatial discretization

The discrete pixel structure leads to spatial digitization of the SLM and the 10-bit addressesd SLM generates 1024 phase levels. The effect of the spatial digitization, known as pixelation noise, has been derived by applying the convolution theorem in Section 1.3 in [35], which turns out to be a sinc function[1] in far field (Fourier plane). The diffracted intensity is thus globally sinc^2-weighted. This weighting can also be seen in the so called first-order diffraction efficiency (DE) curve of blazed gratings as a function of the reciprocal value of P, the pixel number per ramp. To avoid the zeroth-order beam in the holography, blazed phase gratings superimposed on the desired phase pattern are used and they diffract the intensity pattern to other positions[2] in the Fourier plane. The theoretical DE of a blazed grating written on the SLM for q^{th} diffraction order is given by the equation

$$\eta_q = \text{sinc}^2\left(\frac{q}{P}\right) \frac{\text{sinc}^2(q - \Phi/(2\pi))}{\text{sinc}^2(\frac{q-\Phi/(2\pi)}{P})}\,, \tag{4.2}$$

with Φ denoting the peak phase and P the number of steps per period [36, 37]. For the first order and a modulation height of 2π, Equation 4.2 reduces to

$$\eta_1 = \text{sinc}^2\left(\frac{1}{P}\right)\,, \tag{4.3}$$

and is shown in Figure 4.2. The larger the step number per period is, the higher the DE will reach. For example, the DE of a 4-step blazed grating theoretically reach 81%, and an 8-step grating 95%.
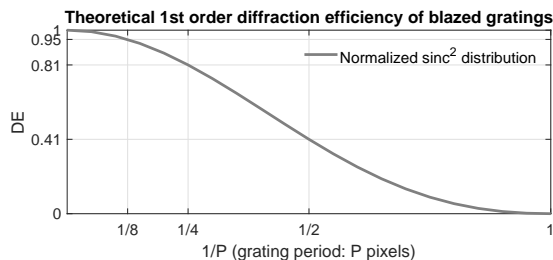

Fig. 4.2: First-order DE curve of ideal blazed gratings.

---

[1] Note that the Fourier transform of a square pulse is a sinc function. [2] Off-axis.

4.1.3 Flickering

To prevent damage to the LC cells, frequently flipped fields are applied instead of a static electric field. The relaxation movements of the LC cells may cause an oscillation in amplitude and phase of the diffracted patterns, referred to as the flickering effect which can be described as a low pass in time and is related to the system's response time [35, 38]. Santec SLM-100 has a response time of ∼ 100 ms according to the operational manual.

4.2 Manufacture-limited electrical and physical phase errors

4.2.1 Flatness error of SLM layers

In an LCoS device, a covering glass is assembled in front of the common electrode and the pixelated electrodes are placed on a silicon backplane, see Figure 4.3. Conditioned on the manufacturing process, both SLM [35] and digital micromirror device (DMD) [39] may have bent physical layer of several λ, even if there is no voltage applying to the devices. An engineer from the company Santec has revealed the producing procedure of the display during his visit to the quantum walk lab. The manufacturer usually overfills liquid crystals between both electrodes in order to achieve high fill factor. As the consequence, the display is bent. A correction kinoform is sometimes directly acquirable from the manufacturer; if not, it can be measured by the customers. There are several diverse approaches to measure the flatness error, including and phase-shifting interferometry [35, 40] and diffraction-based measurement[35, 41]. The correction kinoform is just the inverse of the measured curvature.

4.2.2 Non-linear and inhomogeneous phase response

We have already mentioned that the SLM modulates the phase of incident light by altering the refractive index, see Equation 4.1. Uniform and linear phase response could be expected, if there were no electrical or physical hardware error. This is however barely the case. Non-uniform and non-linear electric driving degrades both the homogeneousness and the linearity of the phase response. In contrast to the non-linearity problem which would require more detailed knowledges on the electric driving scheme, the inhomogeneity problem can be understood by illustration. All pixels in Figure 4.3 are kept DC-balanced, i.e. that the time-averaged applied voltage is 0 V, except for the pixel at position B. Also, thickness variation due to the non-parallel glass substrate and silicon backplane (compare position A and C in Figure 4.3) leads to additional phase delay and contributes the inhomogeneity of the phase response. A multi-dimensional look-up table (LUT) containing these informations is thus crucial for addressing the desired phase on the SLM correctly.
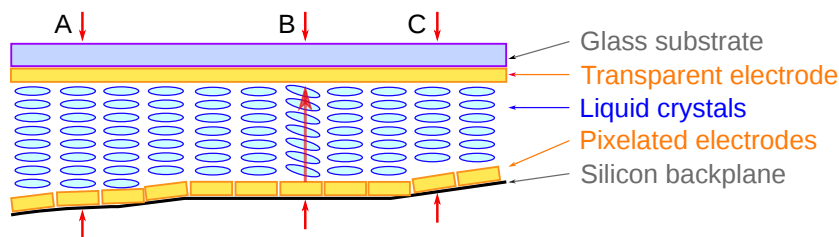
Fig. 4.3: Highly illustrated framework of a PAN LCoS spatial light modulator. The thicknesses of the SLM at positions A and C are different due to manufacture imperfection. All pixels bear zero potential difference, except for pixel at B. This draft is inspired by [43].

4.2.3 Inter-pixel cross-talk effect

The fringing field effect is highly present in LCoS displays. This effect is referred to as the cross-talk between neighboring pixels which arises if significantly different phase/voltage values are applied to the adjacent pixels, leading to the broadening of the phase profile [44, 45], see Figure 4.4. Phase

retardation is not constant over the entire pixel area and the smoothening effect at the edges acts as a spatial low pass filtering of the phase retardation expected for an SLM without inter-pixel cross-talk. This effect can be modeled as a convolution of the ideal phase with a spatially invariant kernel which represents the inter-pixel cross-talk [42]. The kernel can be chosen to be a Gaussian or a generalized Gaussian function. In this work, a Gaussian has been chosen to simulate the inter-pixel cross-talk effect and to compare the simulated smoothened phase profiles with the measured ones (next section).
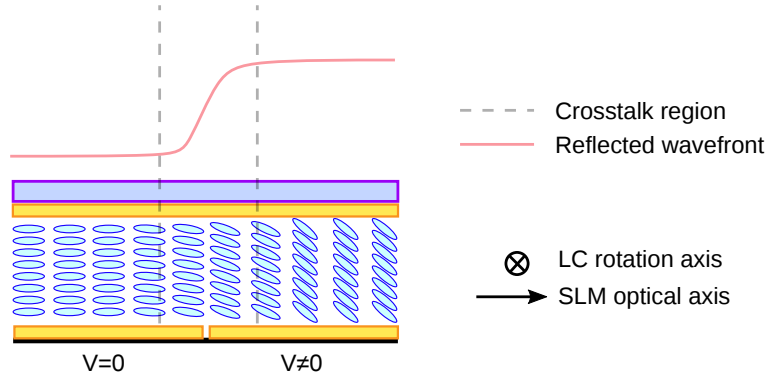
Fig. 4.4: Illustration of the cross section of two adjacent pixels. The electric field applied on a pixel is not limited to the area of that pixel, therefore the molecules near the border of the neighboring pixel are influenced (fringing field effect), causing a smoothened phase profile. This draft is inspired by [46].

4.3 Characterization and compensation

Before the holographic application of the LC-SLM, phase errors discussed in the Section 4.2 should be measured and, if necessary and applicable, compensated. This is a prerequisite of the successful holographic projection. Phase-shifting interferometry (PSI) is applied for the curvature measurement in this work and diffraction-based method is used to reviewed the achieved flatness in Section 4.4 before holographic applications. In this section, the measurement of the SLM surface information and the establishment of the LUT of the phase response will be demonstrated, followed by a discussion of the measured residual phase error. The cross-talk effect will be qualitatively investigated in the spatial domain. The correlation between the inter-pixel fringing field effect and diffraction efficiencies of blazed gratings will be discussed in this spatial analysis and later verified in Section 4.4.3 based on holographic measurements.

4.3.1 Determination of SLM curvature

To determine the wavefront distortion resulting from any curved physical layers of the SLM, the device in OFF state (i.e. grayscale level of zero) is placed in one of the arms of a Twyman-Green interferometer, with a reference piezo-driven mirror in the other arm, see Figure 4.5. Before entering the interferometer, the incident beam has been expanded via two sets of amplification telescopes (L_1 and L_1, L_3 and L_4) by 30 times. The widening approximately enables a flat incident wavefront onto the SLM. The interferograms are projected through a third telescope (L_5 and L_6) onto the camera[1], with the SLM (the mirror) and the camera fulfilling the 4f arrangement. The third telescope is a reducing one due to the finite dimension[2] of the CCD-chip, implying that the Nyquist sampling condition is not fulfilled here. Nevertheless, for a global curvature determination in the order of $\sim \lambda$, a non-linear coordinate transformation[3] relating the CCD coordinates and the SLM coordinates will be sufficient to estimate and recover the aliasing.

---

[1] Thorlabs 8-bit CMOS camera DCC1545M, loosely called CCD in the following context.   [2] CCD-chip size: 1280×1024 pixels; CCD pixel size: 5.2 μm. SLM-chip size: 1440×1050; SLM pixel pitch: 10.4 μm.   [3] The measured surfaces in CCD coordinates are mapped into the SLM coordinates using the MATLAB function `fitgeotrans`.
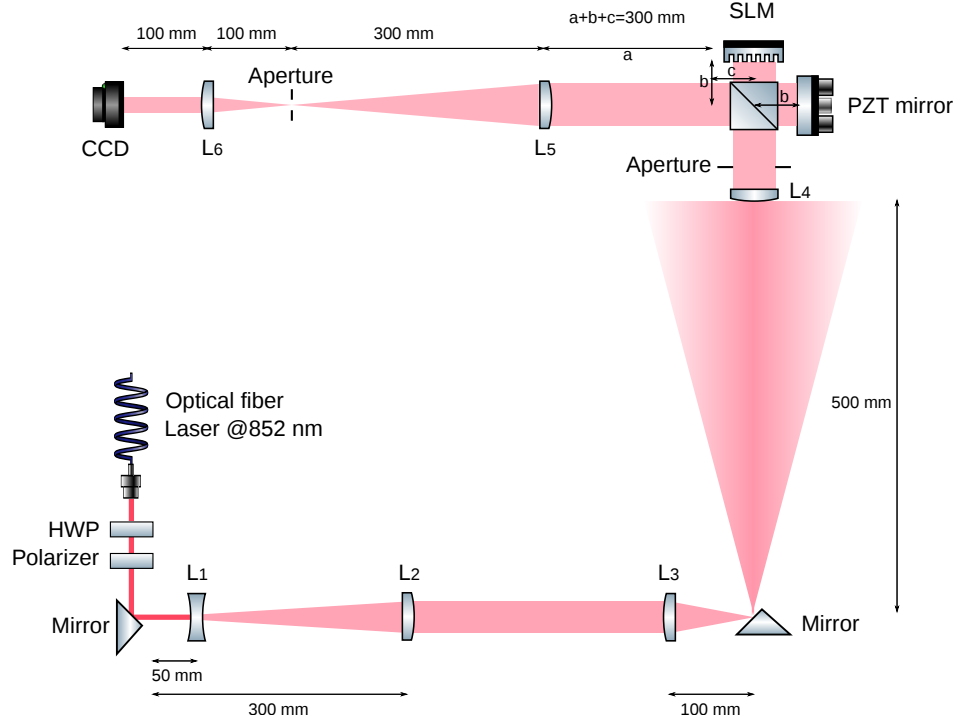
Fig. 4.5: Setup: phase-shifting interferometric measurement of the SLM curvature. An 852 nm laser beam coming out from an optical fiber is first collimated and its polarization is optimized by rotating the half-wave plate and the polarizer after the fiber. To obtain a flat incident wavefront at the SLM stage, two set of amplification telescopes (L$_1$ and L$_1$, L$_3$ and L$_4$) are inserted between the laser source and the interferometer. The interferograms are than projected through a reduction telescope (L$_5$ and L$_6$) onto the CCD-chip. The piezo reference mirror, the SLM and the CCD camera are controlled via computer software.

The interferometric method bases on the theory of two-beam interference, for example a Michelson interferometer or its variant the Twyman-Green interferometer. The output intensity of such an interferometer is given by

$$I_{\text{int}} = I_1 + I_2 + 2\sqrt{I_1 I_2} \cdot \cos(\Delta\Phi), \tag{4.4}$$

with I_1 and I_2 the stationary components of both arms and the last term the crossing term. $\Delta\Phi$ denotes the phase difference of two arms, which can be divided into the phase difference $k \cdot \Delta\phi$ resulting from the path difference (variable by shifting the piezo-driven reference mirror, $k \in \mathbb{N}$) and the fixed term ϕ resulting from the any non-flat surface. Treating $I_1 + I_2$ as some intensity offset O and $2\sqrt{I_1 I_2}$ as the interference amplitude A, the Equation 4.4 can be rewritten in

$$I_{\text{int}} = O(x, y) + A(x, y) \cdot \cos(k \cdot \Delta\phi + \phi(x, y)), \tag{4.5}$$

where (x, y) denotes the CCD pixel coordinates in the PSI scheme[1]. Calibrating the frequency $\Delta\phi$ per step[2] and applying a pixel-wise cosine fitting to the single snapshots, the three parameters O, A and ϕ can be obtained, see illustration in Figure 4.6.

---

[1] The SLM coordinates are denoted as (X, Y) in this context. Both CCD plane and SLM plane are in spatial domain. [2] By means of the MATLAB function `rootmusic`.
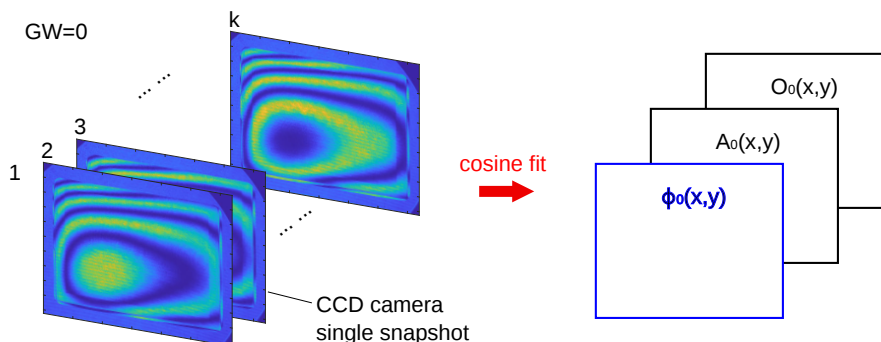
Fig. 4.6: Scheme of PSI for measuring the SLM curvature. A series of interferograms are measured as the function of piezo-driven reference mirror shifting step k. The SLM is in OFF state. A pixel-wise cosine fitting gives the three fitting parameters, where $\phi(x, y)$ is the required curvature information. The index 0 in the three parameters indicates the voltage OFF state of the SLM. "GW" denotes the grayscale value sent to all SLM pixels.

This technique is convenient without involving complex phase retrieval algorithms, i.e. the phase information is directly obtained in the spatial domain. But one disadvantage of this approach is that any imperfection of the beam splitter or/and reference mirror introduces new aberration into the measured result; imperfect alignment could also lead to slight defocus and astigmatism. However, such additional optical aberrations are able to be corrected by further approaches such as diffraction-based method, depending on the precision required in the individual experiment. An unwrapping technique is required during the evaluation because of the 2π-ambiguity of cosine functions. In this work, the Ghiglia-Romero 2D unwrapping algorithm [51] is chosen to unwrap the phase in all PSI measurements. The robustness of the frequency calibrating method, the pixel-wise cosine fitting of surfaces and the unwrapping method has been proven by synthetic surfaces. In addition, the sensitivity of the interferometer to differential path and common path was also qualitatively reviewed, see Figure 4.7. After the three parameters (Figure 4.8) are acquired, the phase map $\phi_0(x, y)$ has been unwrapped and transformed into the SLM coordinates (X, Y), then inverted and fitted by a 2D polynomial smooth surface, which serves as the compensation mask, see Figure 4.9. The PV value of the measured curvature is 2.14λ, lying in the expected range[1].
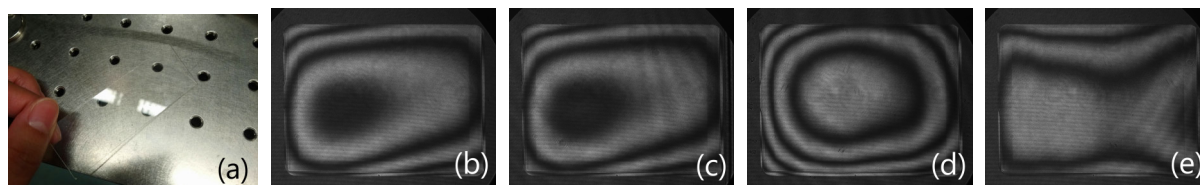
Fig. 4.7: Testing the sensibility of the interferometer. An old transparent attenuator (a) was placed into the common path (c), the mirror arm (d) and the SLM arm (e). It can be seen that the interferogram is sensitive to phase differences in differential path, but not sensitive to phase distortion in the common path, comparing with the situation that no attenuator is present (b).

---

[1] The company Santec has revealed that the curvature is $> 2\lambda$.
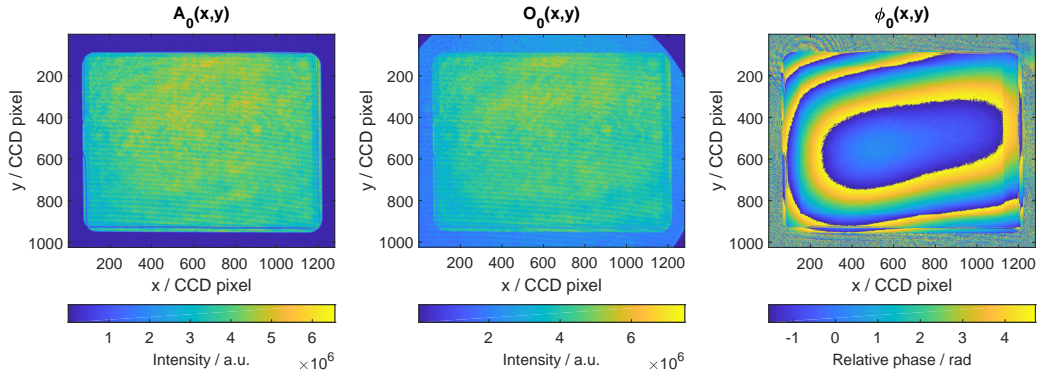
Fig. 4.8: Three parameters of the cosine fitting during the wavefront measurement.
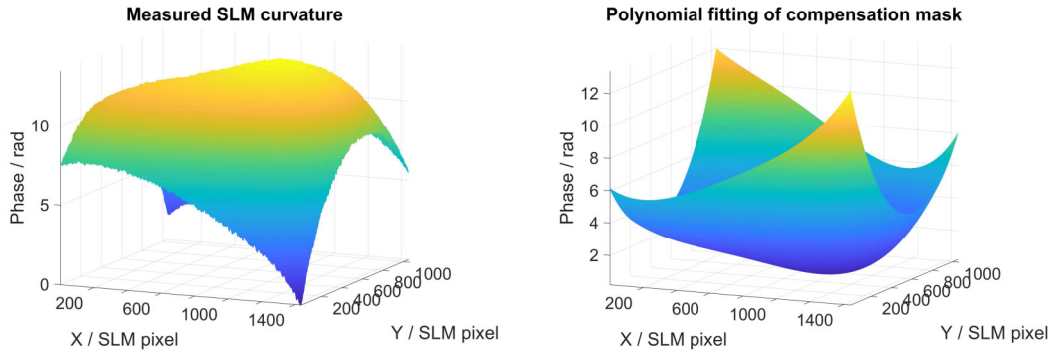
Fig. 4.9: Measured curvature of the SLM (left) and the compensation mask (right).

4.3.2 SLM Gamma test

To create a correlation between the SLM voltage levels, which are mapped in grayscale levels via the SLM hardware, and the modulated phase for the wavelength of 852 nm, the LC-SLM gamma curve needs to be calibrated. Some authors have suggested the SLM display be divided into two areas and brought into interfering with itself (diffraction-based, zeroth-order beam with first-order beam [35, 47]) or with a reference flat surface (interferometric [48]), simply assuming that all SLM pixels behave in the same sense. Measuring the shifted positions of the interference fringes as the function of the relative grayscale level between both SLM areas would deliver the overall gamma curve of the SLM. But considering the inhomogeneity of the phase response discussed in Section 4.2, a pixel-wise treatment is strongly recommended. This is easily achieved by just extending the curvature measurement from the SLM OFF state to the entire grayscale range, explained in Figure 4.10.
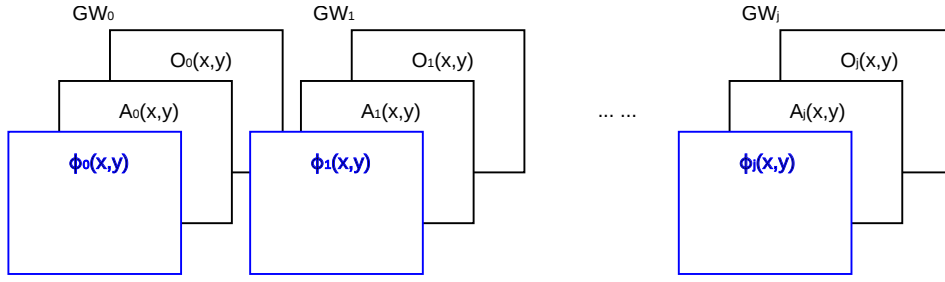
Fig. 4.10: Scheme of PSI for measuring SLM gamma curves. Using the same method introduced above, a series of cosine fitting parameter sets are evaluated as the function of equidistantly spaced grayscale levels GW.
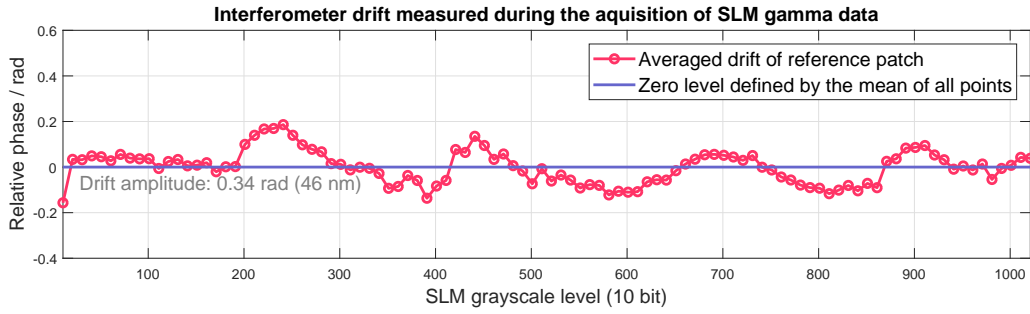
Fig. 4.11: Inteferometer drift.

The measurement was carried out in the entire grayscale range in step of 10 and it took 45 minutes. Therefore the spatial drift of the interferometer needs to be measured and subtracted, in order not to influence the measured phases. This is done by leaving a small patch at one of the corners of the SLM matrix being in the OFF state during the entire measurement. The averaged fluctuation in this patch as a function of time/step is shown in Figure 4.11. After the drift subtraction, the relation between modulated phase and the SLM grayscale level can be established. Depending on the precision and efficience required for further experiments, different models can be applied.

Linear and non-linear models

To visualize the gamma curve, the phase offset $\phi_0(x, y)$ is subtracted and the modulated phase for each grayscale level is averaged, except for the pixels in the reference patch. Plotting the averaged modulated phases against the corresponding grayscale levels yields the overall gamma curve, see the blue curve in Figure 4.12. Apart from the saturation region which begins from grayscale level 950, the measured overall gamma curve shows a sound linearity. A linear regression with the goodness of fit (GOF [52]) of 0.99977 and the deviation of single point from it are presented in Figure 4.12 and Figure 4.13, respectively.

The linear regression has also been carried out for each pixel except for the reference patch, since some details might have been averaged out in the overall test. The pixel-wise linearity analysis produces the same average value of the slope, namely 14.1 mrad/grayscale level. The distribution of the individual slopes was not Gaussian based on a pre-analysis. The distribution of the GOF for all involved pixels is shown as Histogram 1 in Figure 4.14, with a mean value of 0.99926. These indicate that the phase response is neither uniform nor linear. The SLM display is not only bent, but also has a slight spatial thickness variation. The PV value of the residual phase error after compensation measures $\lambda/7$ in case of the overall and individual linear models. To achieve precision calibration, a polynomial model up to the 9th order is adopted, such that the residual PV value can be reduced to $\lambda/15$. Also, Histogram 2 in Figure 4.14 and the comparison of both histograms in the same axes

scaling show that the polynomial model is far more appropriate than the linear model, having a mean GOF of 0.99997. Despite of the increased complexity of the polynomial fitting, the increment of computational time is only of factor 2. On a conventional PC with Intel® Core™ *i*5 processor and 8 GB RAM, the LUT calculation takes 0.2 second for each hologram using the linear model, and just 0.4 second if using the polynomial model.
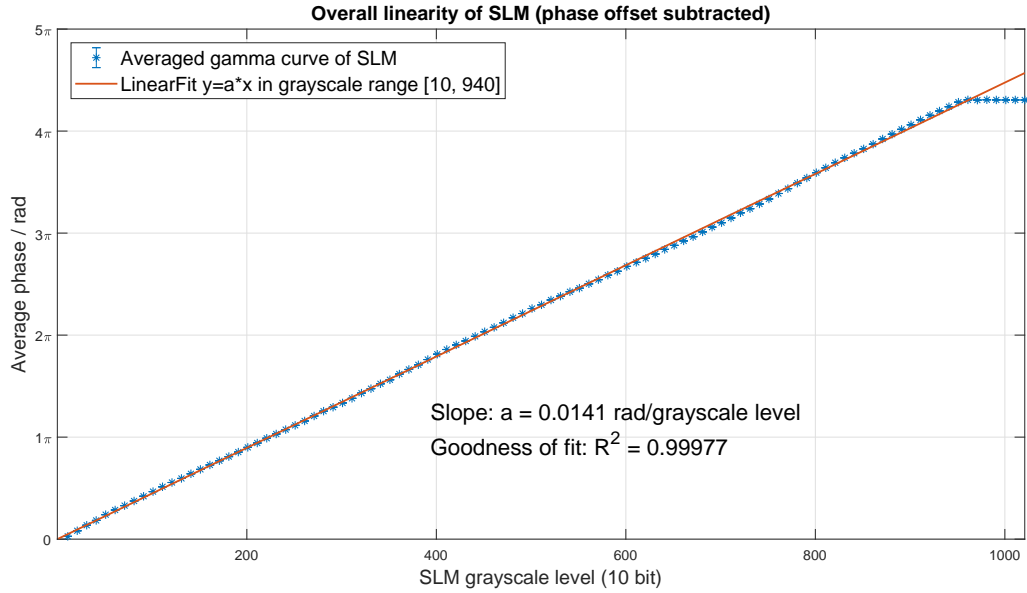
Fig. 4.12: Averaged overall gamma curve of the SLM phase response.
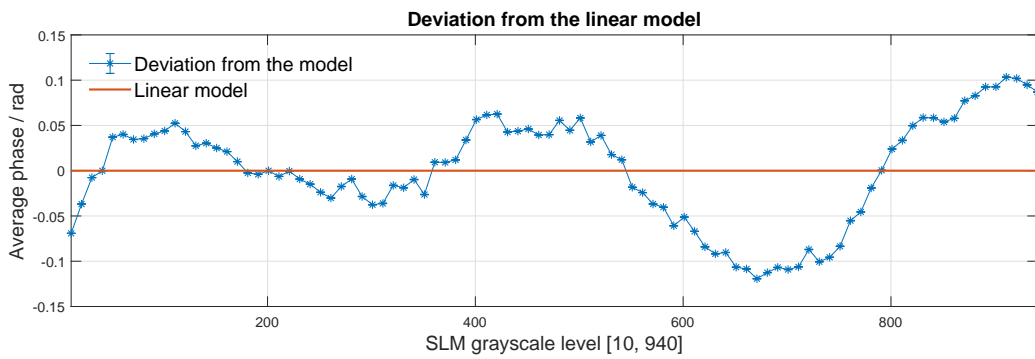
Fig. 4.13: Deviation from the overall linear model.
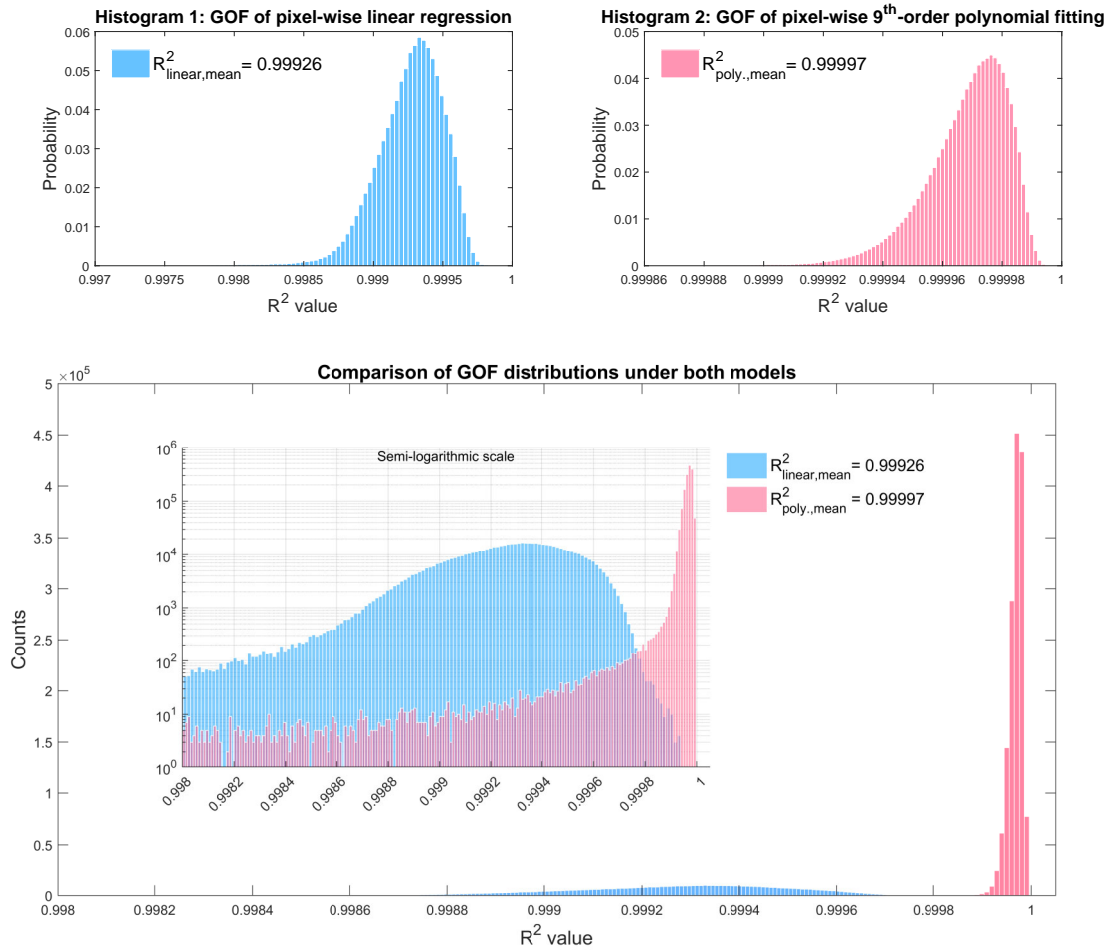
Fig. 4.14: Upper: goodness of fit distributions of pixel-wise linear model and polynomial model. Lower: comparison of both histograms in the same axes scaling. Comparing to the linear model, the GOF distribution of the polynomial model is narrow and very close to 1.

4.3.3 Residual phase error measurement
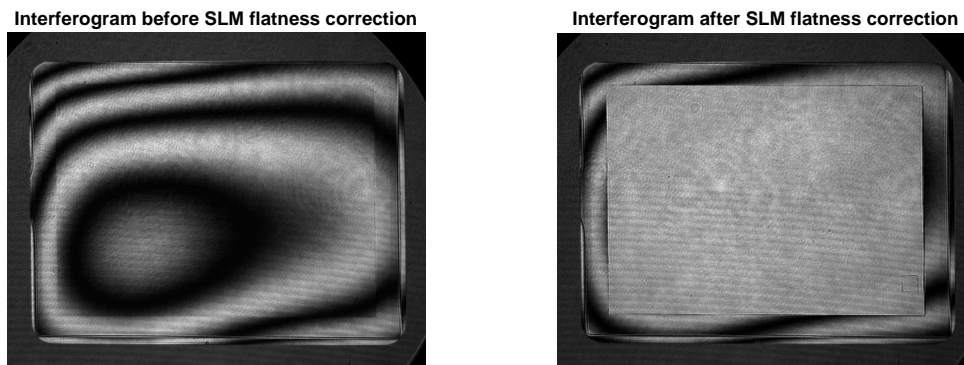
Fig. 4.15: Camera pictures before and after SLM compensation.

The compensation mask in unit of radian is translated into grayscale level via the LUT obtained in

the polynomial model and sent to the SLM. The flattening effect is enormous, see the comparison in Figure 4.15. The compensated surface is measured again and compared with the uncompensated surface in the same axes scaling in Figure 4.16. The flatness RMS of the corrected wavefront measures $\lambda/78$.
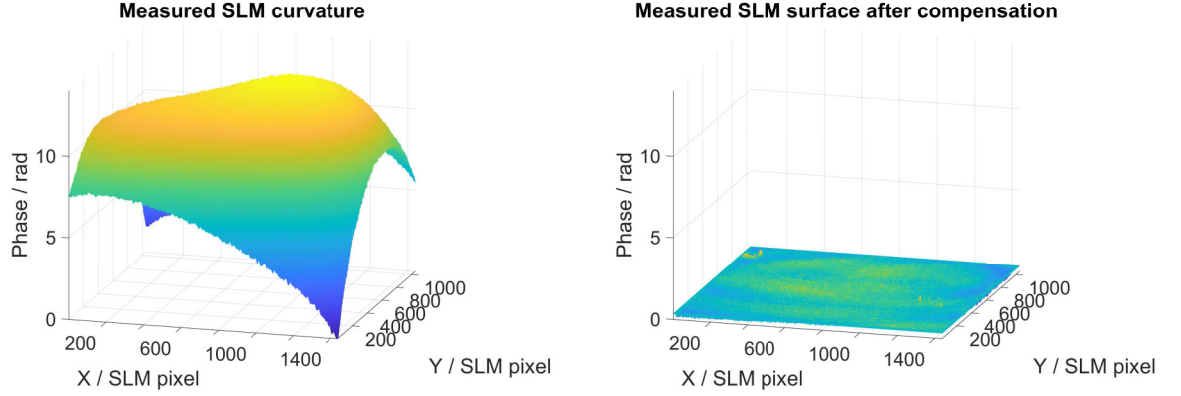
Fig. 4.16: Measured wavefront before and after SLM compensation.

4.3.4 Qualitative investigation of inter-pixel cross-talk

In the framework of PSI, the cross-talk effect can be investigated in the spatial domain by replacing the reduction telescope (L_5 and L_6 in Figure 4.5) with an amplifying one. A 10 times amplification is suggested in [42]. In our experiment, a telescope with an 80 mm lens and a 1000 mm lens providing 12.5 times amplification was used, such that one SLM pixel was projected onto 25 CCD pixels. Observation in the spatial domain however only provides an estimation of the inter-pixel cross-talk effect, because the smoothened phase gets convolved with the point spread function (PSF) of the imaging system again and thus becomes broader in the observation plane. In practise, low-order optical aberrations such as defocus and astigmatism can hardly be avoided, making the situation worse. Nevertheless, the cross-talk effect under the additional influence of an ideal PSF can still be roughly simulated.

The vertical direction

This measurement was carried out separately in the vertical and horizontal directions. Three phase patterns were selected and sent to the SLM: a binary phase step of 1.5π, a single pixel lifted by 1.5π comparing with its neighbours and four 8-step 2π ramps, all along one direction. The wavefronts were measured by PSI again and the average values along the perpendicular direction is calculated. The 1D phase profiles (blue curves in three sketches in Figure 4.17) were obtained by this mean. The NA of the amplifying telescope is 0.16[1] and the associated ideal PSF with an Abbe radius $r_{Abbe} = \lambda/(2\mathrm{NA}) = 0.26$ SLM pixel is shown in the left sketch of Figure 4.18. Under this model, the blurred phase profiles without cross-talk effect (yellow curves in Figure 4.17) and under cross-talk effect (magenta curves in Figure 4.17) are simulated and can be compared with the measured ones. The width of the assumed Gaussian kernel is adjustable and controls the broadening of the phase profiles. In this visual comparison, the Gaussian width σ is optimized at 0.2 SLM pixel, shown in the right sketch in Figure 4.18. That optical aberrations cannot be totally eliminated in practise, indicates that the width of the Gaussian kernel is smaller than 0.2 SLM pixel.

---

[1] Diameter of the 80 mm lens is 25.4 mm.
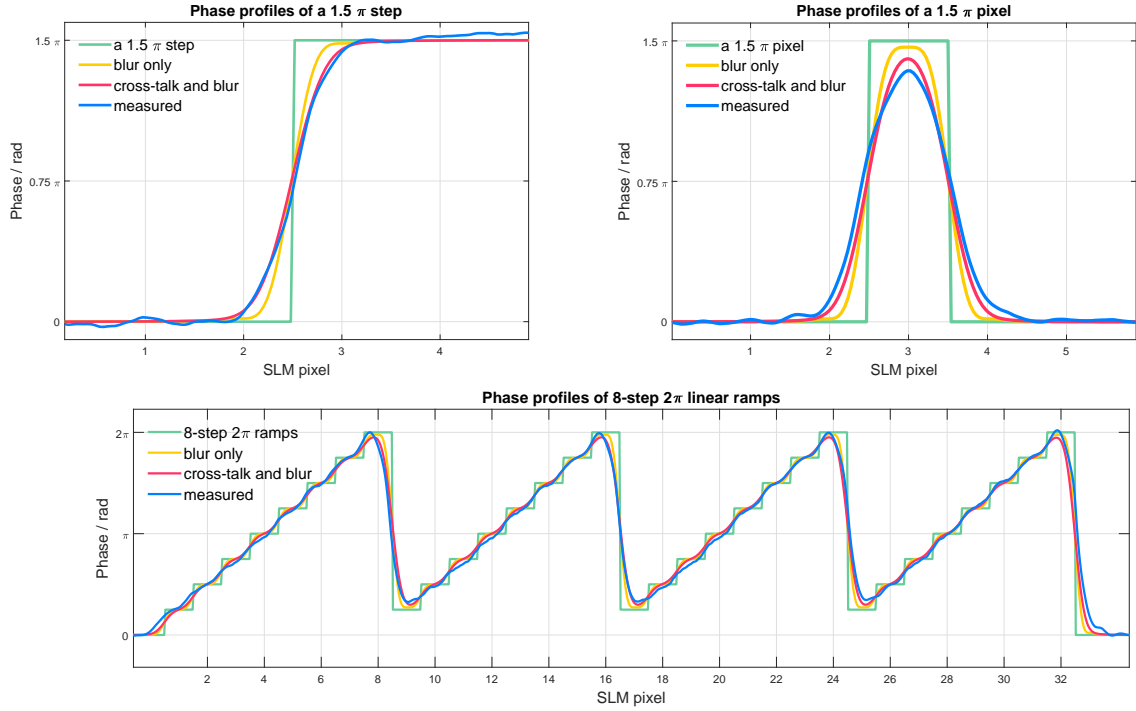
Fig. 4.17: Simulated and measured phase profiles.
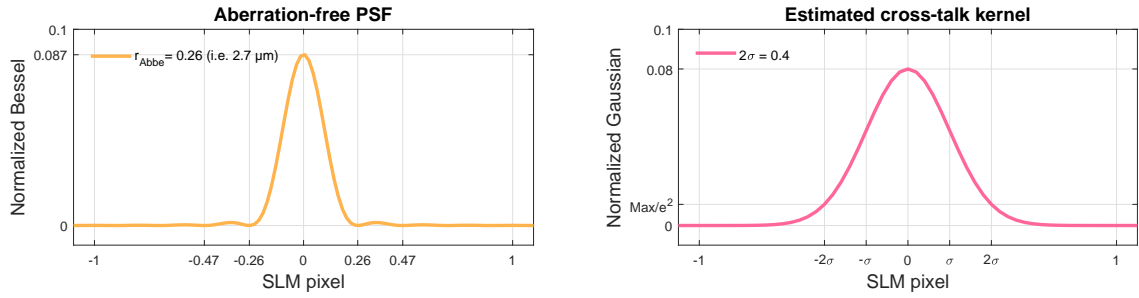
Fig. 4.18: Estimated kernels of the imaging system and the cross-talk effect.

There are two consequences of the cross-talk effect, which counteract each other:

- for continuous phase structures, e.g. the ramps of blazed gratings, the smoothening effect actually enhance the DE, because it suppresses the discretization;

- for the phase jumps $2\pi \rightarrow 0$, this smoothening effect sends light to unwanted directions and hence reduces the DE.

As a net result of these two facts, it can be expected that the first-order DE curve of blazed gratings deviates from the theoretically predicted one in this way: the smaller the pixel number P per ramp is, the smaller its DE will be. We will confirm this expectation with experimental data in Section 4.4.3.

The horizontal direction

As a consequence of the anisotropic arrangement of rod-shaped LC molecules in one SLM pixel and hence probably different magnitudes of the fringing field effect in vertical and horizontal direction, a disparity in measured diffraction efficiencies of the two directions could be expected. Indeed, this DE disparity was observed in [36] and [42]. Unfortunately, the same measurements and analysis in the horizontal direction were not possible for the Santec SLM-100 due to some unclear electric/electronic

driven scheme of the display. A report on this issue is attached separately and has been sent to the manufacturer. The device was also sent to Japan for investigation, after all holographic data were acquired.

4.4 Investigation in Fourier domain

The SLM flatness correction and phase response calibration have been done with a satisfying result, but it's still interesting to know if the achieved flatness satisfies the condition of a diffraction-limited system, when the setup is changed. This is important for the final goal of this work - reconstructing structured intensity patterns with the pre-calculated holograms. For this purpose, doughnut modes introduced in the earlier chapter come back to the play. The telescope between the SLM and the camera is replaced by a 2f-correlator with focal length $f = 150\,\text{mm}$ and the beam in the reference mirror arm of the interferometer is blocked. An Iris aperture was placed in front of the SLM display to create a circular aperture which covered the 700×700 pixel hologram matrix. Holograms containing the SLM compensation mask, spiral phases with topological charge $l = \{0, 1, 2, 3\}$ and a 64-step blazed grating are transferred to the SLM. Diffracted patterns in the conjugate plane (camera) are measured as single snapshots.

4.4.1 Creating an Airy disc (LG$_{00}$ mode)

[30] has demonstrated a method based on Fourier optics to evaluate the measured Airy disc and to estimate the phase error of wavefront at the aperture. The essential idea is to estimate the NA in the Fourier domain by the Abbe cut-off of the modulation transfer function (MTF). High-frequency noise can be Fourier filtered out and data can be interpolated according to the Whittaker-Shannon interpolation theorem. The Airy disc is here the ground LG mode with topological charge $l = 0$. Figures 4.19 and 4.20 show the raw data and interpolated data of the LG$_{00}$ mode in 2D and 3D, before and after the SLM correction. The second maximum of the correlated Airy disc can be clearly seen, while the uncorrected mode does not even have the Airy disc form - totally distorted. The Strehl ratio of the corrected LG$_{00}$ mode reaches 82%, fulfilling Maréchal's criterion[1]. The uncorrected mode only has a Strehl ratio of 24% - this persuasively explains why it's so important to calibrate the SLM before any further holographic application. The MTFs and PSFs of both cases are both shown in Figure 4.21.

---

[1] According to Maréchal's criterion, a system can be considered as diffraction-limited, if the Strehl ratio is not less than 80%.
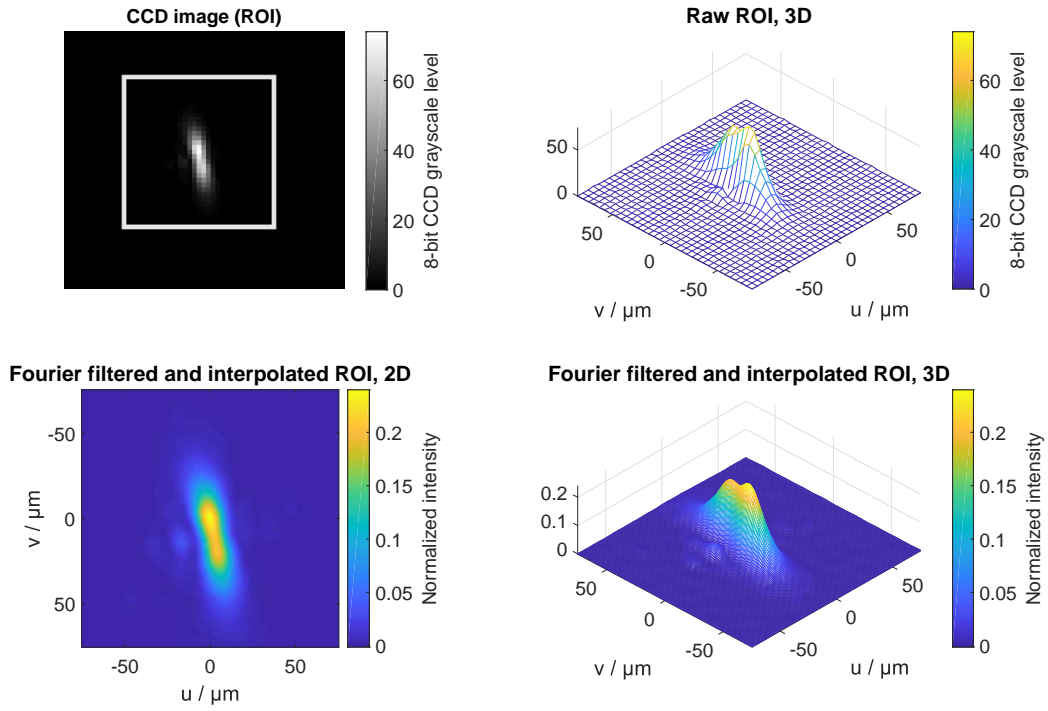
Fig. 4.19: Measured Airy disc (LG_{00} mode) before SLM compensation.
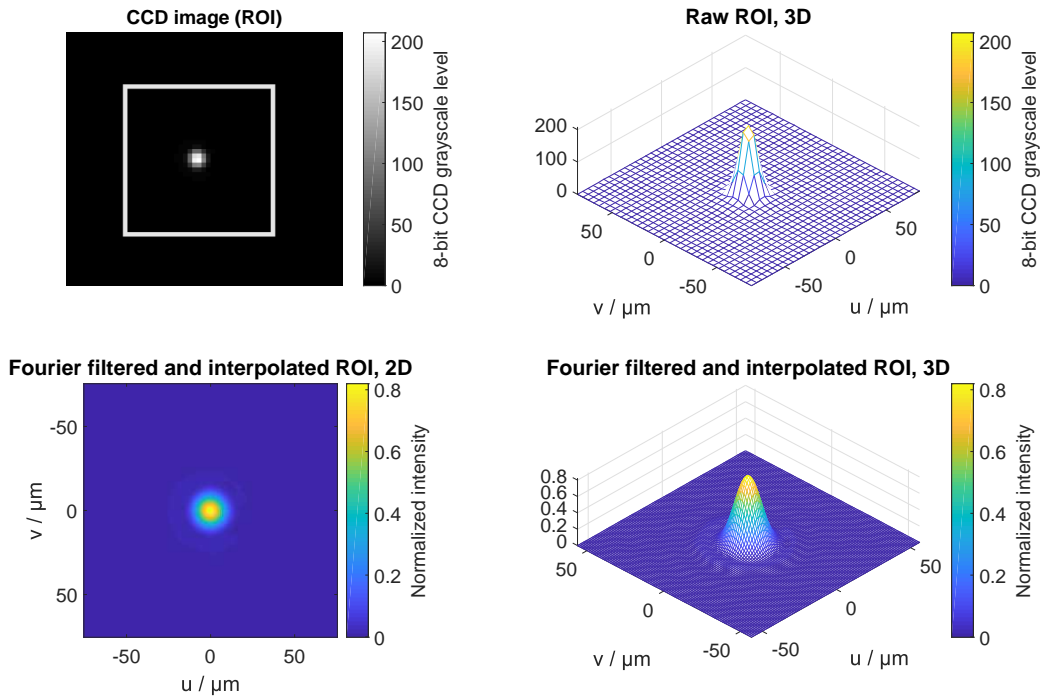
Fig. 4.20: Measured Airy disc (LG_{00} mode) after SLM compensation.
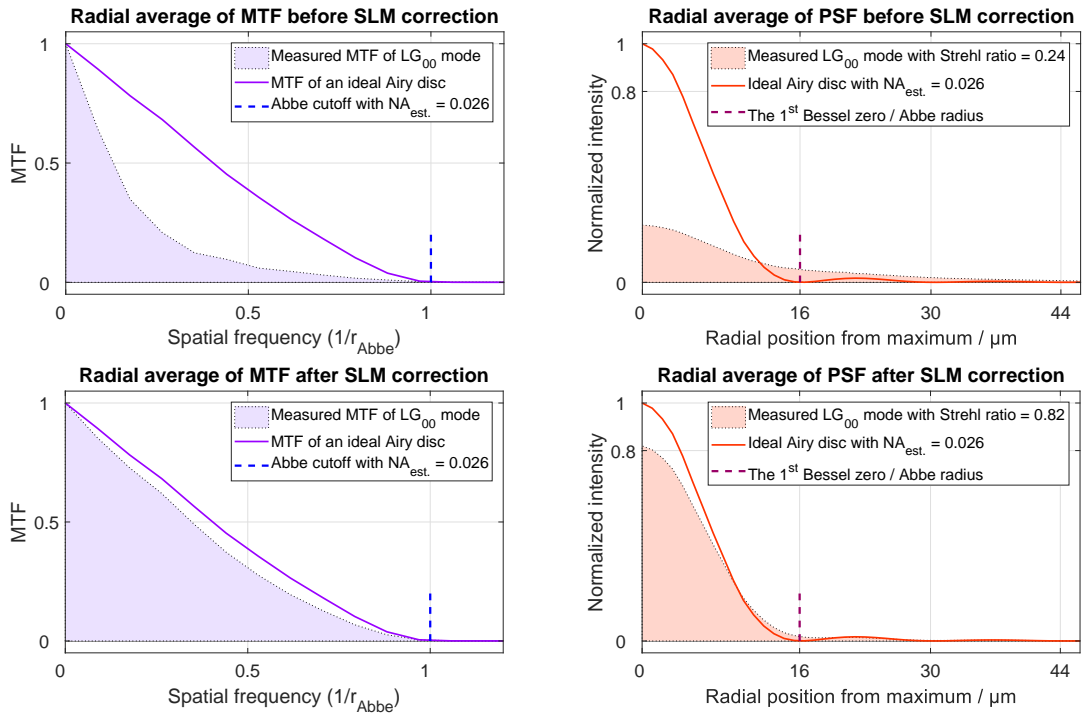
Fig. 4.21: Evaluated modulation transfer functions and point spread functions. Upper: before SLM compensation. Lower: after SLM compensation.

4.4.2 Laguarre-Gaussian modes

Remarkable differences can also be observed for the other LG modes, see Figure 4.22. The measured modes are displayed in colormap such that the second maxima can be clearly seen. The correlated doughnut modes agree with the numerical simulations in Figure 2.2 extremely well and this again confirms the fidelity of the SLM compensation.
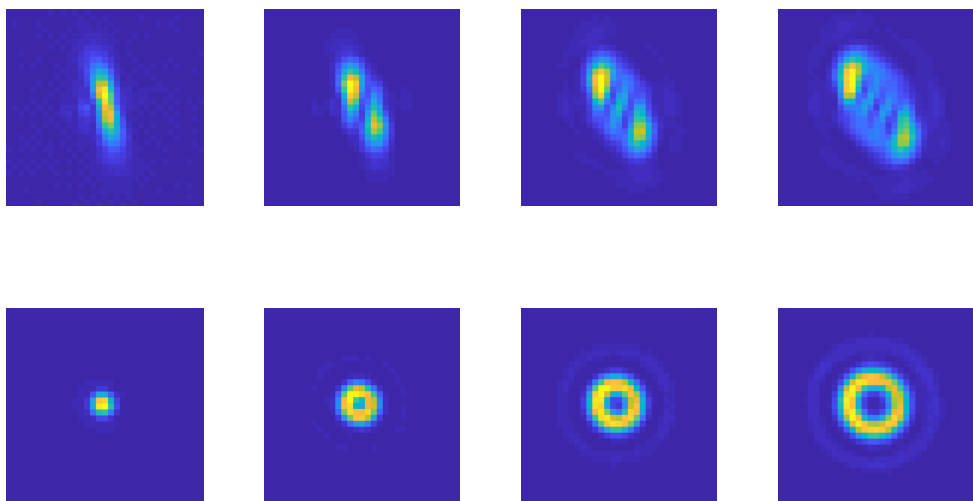
Fig. 4.22: Uninterpolated CCD pictures of LG modes in colormap before (the 1st row) and after (the 2nd row) SLM compensation.

4.4.3 Measuring DE curves

The pixelation problem and the cross-talk effect which affect the DE have already been theoretically discussed in previous sections, to investigate this issue, I measured the ratio between the intensity of the first-order pattern and the intensity of the zero-order pattern when no grating is applied, and defined this ratio as the diffraction efficiency (DE) in this context. The measured DEs of a series of vertical blazed gratings are plotted and compared with the theory curve in Figure 4.23. The expected deviation from the theory curve is observed: as P is decreasing, the DE decreases off the theory curve too. For a good performance of the holographic projections, a blazed grating with more than 8 steps is recommended.
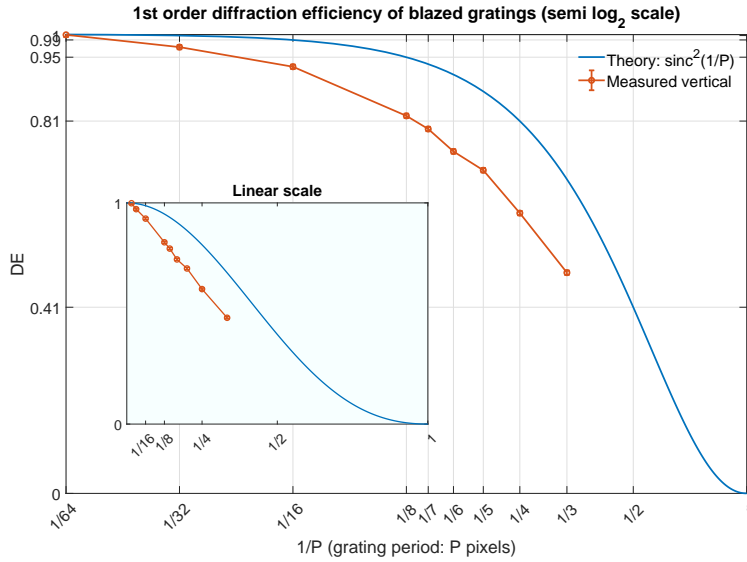
Fig. 4.23: Theoretical and measured DE curve.

Another factor that affects the DE is the fill factor of the LC-SLM. The theoretical fill factor of pixel size $10\,\mu m$ and pixel pitch $10.4\,\mu m$ is calculated to 92.5%, which means, only 92.5% of the reflected light gets modulated. However, in the fabrication procedure, the display is usually overloaded with LC molecules, also in the gaps between adjacent pixels. Therefore an effectively near 100% fill factor is achievable and this is the case for the 64-step grating (99.84%). After the analysis of the diffraction properties and the acquisition of data for reconstructed intensity patterns (next chapter), the physical lens was removed and a thin lens function with $f = 300\,mm$ was superimposed with the hologram of the LG_{00} mode and SLM compensation mask. In this case, no blazed grating is needed, because the zeroth-order light will not be focused but rather they propagate freely along the optical axis, acting as a very week background in the observation plane. The Strehl ratio is now measured against, (almost) without additional aberration from the supporting optics. The result is 88%, as shown below. The flatness RMS of the wavefront is as expected degraded from $\lambda/78$ to $\lambda/18$, but still lies the safe range.
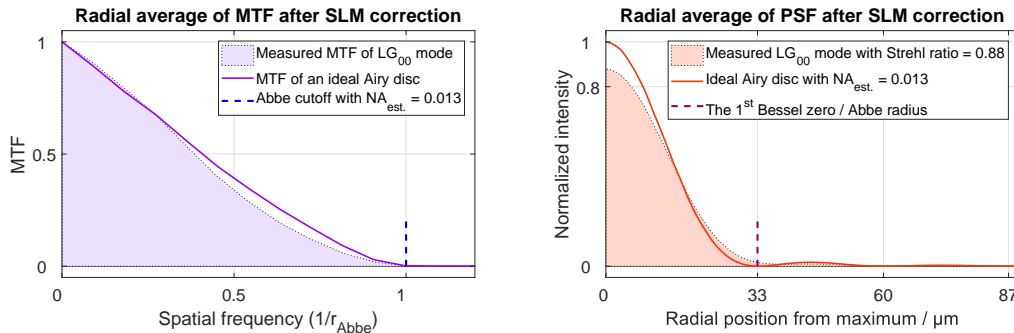
Fig. 4.24: Evaluated modulation transfer function and point spread function after compensation in case of the thin lens function (f=300 mm).

Experimental results and outlook

Now the SLM is prepared for holographic applications. The data measured for both test intensity patterns "plateau" and "ramps" are obtained in the same 2f-correlator for the LG modes measurements. The holographic projection is still taking place in the vertical diffraction direction, but the light reflected by the SLM area outside the 700×700 pixels hologram matrix and inside the larger circular Iris aperture is diffracted into the horizontal direction. This step is optional and moves the light gathering in the zeroth-order position away, such that the target pattern has a relative clean background.

Fig. 5.1: Demo pattern "Averangers" with the zeroth-order spot untouched (left) and with attenuated zeroth-order spot (right). If the zeroth-order spot is too strong, its fringes affect the target pattern. The measured demo pattern has a size of $1.2\,\mathrm{mm} \times 1.2\,\mathrm{mm}$.

5.1 Result of the SOMRAF algorithm

For each test pattern, the pre-calculated hologram is superimposed with the SLM compensation mask and several gratings of different grating periods. The diffracted patterns at the corresponding diffraction positions are measured (Appendix A.2.2) and averaged after careful alignment, such that spatially varying background interferences can be averaged out. The results are displayed in Figures 5.2 and 5.3. Same as the simulations, there is no optical vortex detected. To check the quality of the results, the evaluations of RMS, SNR and resolution discussed in Section 3.1.3 are carried out again for the experimental data. However, due to the blur effect of the imaging system, the regions where the evaluations take place are re-defined, in order to avoid the pattern-background crossover (Figures 5.4 and 5.5). Now the relative RMS of the plateau area of the test pattern "plateau" is measured 7.6% and the SNR 24.1 dB, in the same magnitude of the simulated results (3.9% and 22.5 dB, respectively). In the phase retrieval algorithm, the incident beam was assigned with a flat wavefront and a uniform

intensity, while in practise this was not the case. This contributes to the degradation of the flatness RMS. Also, new phase error has been introduced after the 4f-system was replaced by the 2f-correlator, which affects the quality of the reconstructed pattern as well.
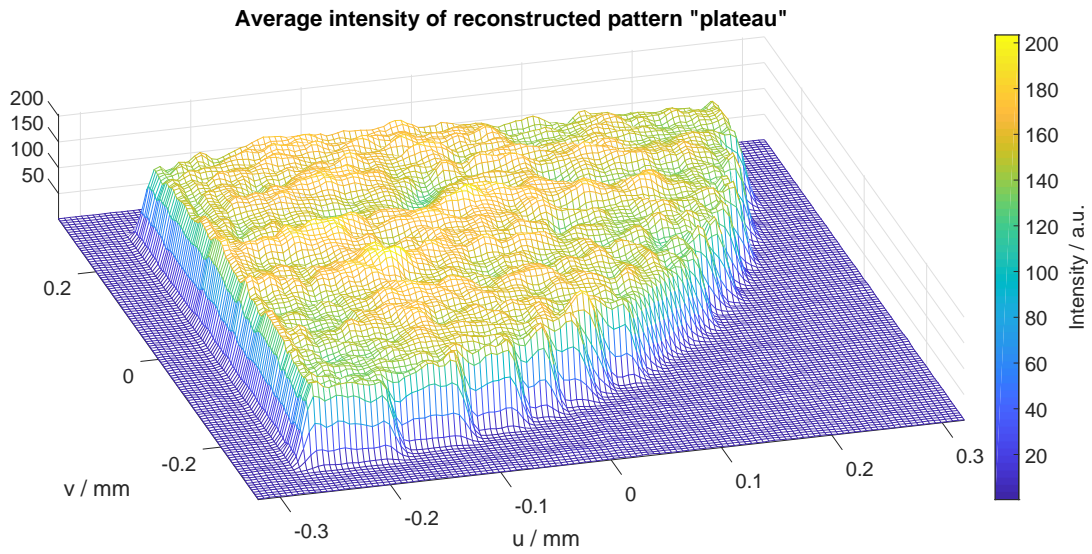
Fig. 5.2: Measured and averaged pattern "plateau".
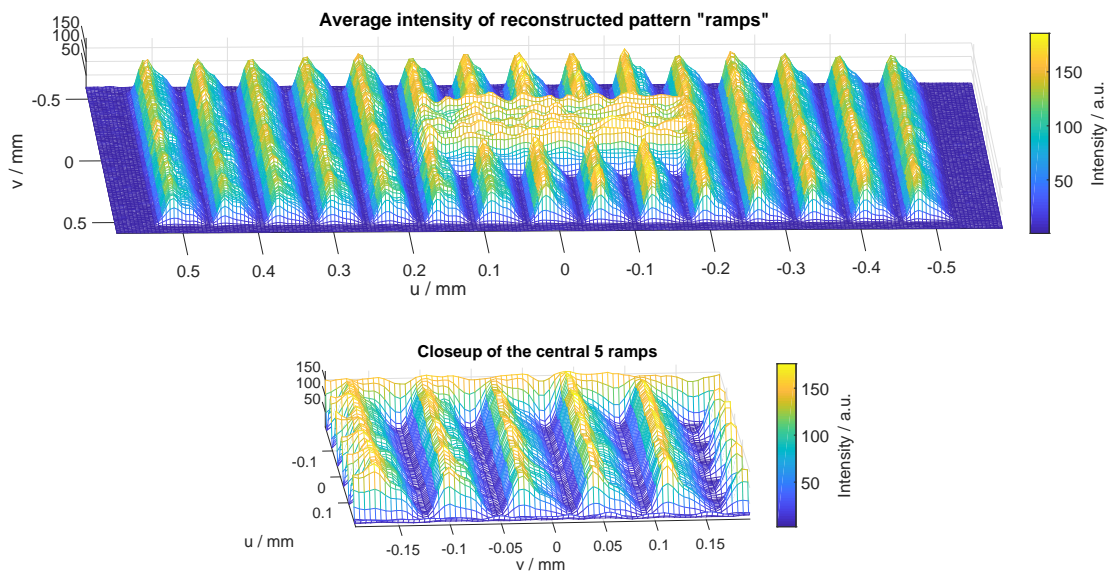
Fig. 5.3: Measured and averaged pattern "ramps".
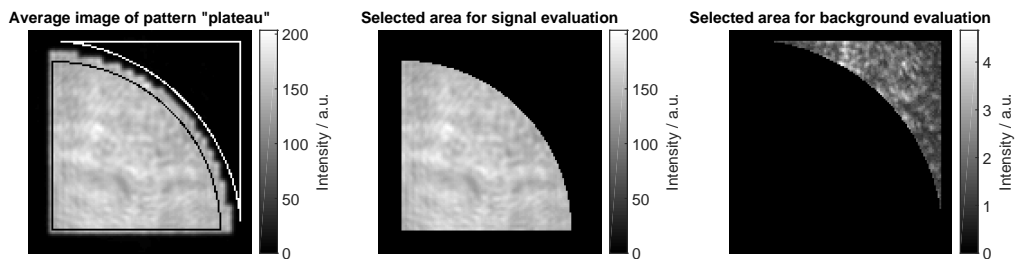
Fig. 5.4: Left: averaged image of pattern "plateau"; the area surrounded with dark line is selected for signal analysis and the area surrounded with bright line is selected for background noise analysis. Middle: selected signal area. Right: selected noise area.

Average image of pattern "ramps"
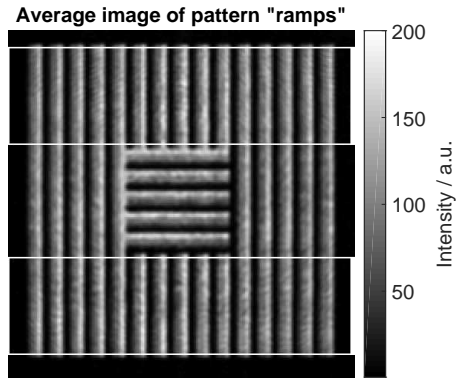
Fig. 5.5: Averaged image of pattern "ramps". The areas in both high-lighted rectangles are used for investigation of achieved resolution.

For the test pattern "ramps", the averaged profile in the selected outer ramps is to be compared with the simulated one. Since each Fourier pixel is projected onto roughly 3 CCD pixels, the simulated data (the 1st plot of Figure 5.6) is first interpolated with a factor of 3 (the 2nd plot of Figure 5.6) before comparing with the measured one (the 3rd plot of Figure 5.6). After translating the Fourier pixel and the CCD pixel into physical sizes, now the simulated and the measured profiles are compared in the 4th plot of Figure 5.6, where a remarkable coincidence is observed. The result of this extreme test pattern has securely confirmed the quality of the SLM characterization and the robustness of the SOMRAF algorithm.
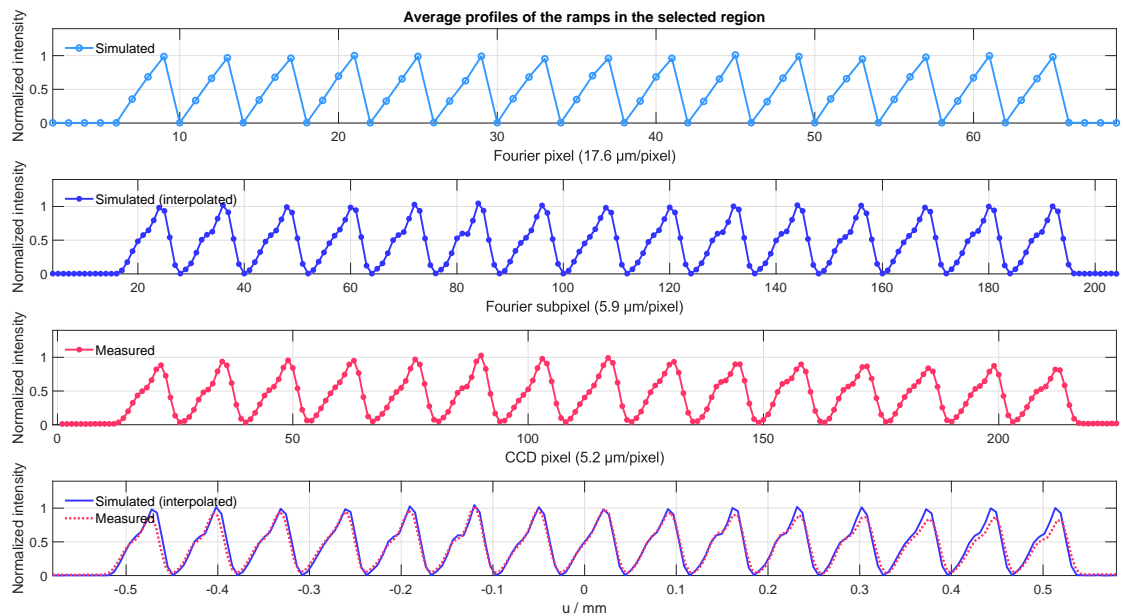
Fig. 5.6: Average profiles of the ramps in the selected region. After interpolation with a factor of 3, the simulated ramps are compared with the measured ones along one direction in the 4th plot. The measured profile coincides with the simulated one very well, except for small deviations in the outer ramps.

5.2 Result of the naïve Gerchberg-Saxton algorithm

For comparison purpose, the GS results were also measured experimentally (Figure 5.7). As discussed and expected, speckles were ubiquitous in the reproduced patterns. Speckles act as scattering centres and make the reconstructed patterns inappropriate for atom confinement experiments.
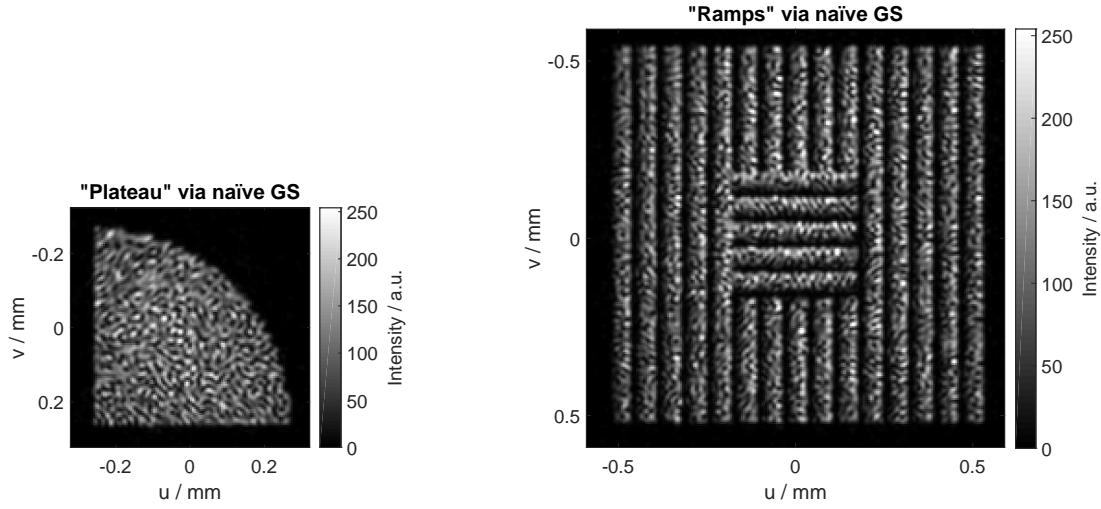
Fig. 5.7: Single images of patterns reconstructed via naïve GS.

5.3 Outlook

The experimental results of reconstructed intensity patterns coincide with the simulations through the SOMRAF algorithm in an accuracy at the percent level. To further enhance the precision, several measures can be taken. There are three main factors that might need some concern:

1. **Spatial information of the incident beam**: the 2f system needs to be extended such that simultaneous spatial measurement is possible;

2. **Presicion phase error correction**: diffraction-based in-situ phase error correction suggest by [35] is suitable for the 2f setup, without further extension;

3. **Global intensity modulation due to pixelation noise**: depending on the sizes of the target patterns, the global $sinc^2$-weighted intensity modulation can be suppressed with the *active feedback* method suggested by [24].

Conclusion

This thesis has presented a journey of the phase retrieval problem starting from a historical and mathematical exploration of the phase problem, followed by the correlation with the task of the topologically protected edge-state analysis in the 2D quantum walk experiment. After investigating the properties and limitations of the widely used phase retrieval method - the Gerchberg-Saxton algorithm, heuristic improving measures proposed by pioneers can be understood based on the underlying physics. As stated in [24], none of the existing GS-like variants is a overall winner in recovering phase (also known as CGH calculation in holography); the performance of the algorithms highly depends on the requirement of the individual experiment, such as relative RMS, spatial resolution, light usage efficiency, temporal stability, etc.. In particular, the SOMRAF algorithm for the quantum walk experiment introduces softness into the iterative routine in oder to prevent fringing artefacts at sharp edges. The reconstructed binary intensity pattern after 200 iteration (1 minute runtime) has a relative RMS of 3.9%, comparing with the OMRAF result 13% with the same parameters.

The holographic projection is also physically implemented using an LC-SLM, after the wavefront flatness error and the inhomogeneous and non-linear phase response are corrected by means of pixel-wise phase-shifting interferometry. The result of the SLM characterization is proven to be reliable, according to both spatial and holographic residual error measurements. The experimentally reconstructed binary intensity pattern has achieved a relative RMS of 7.6% with a sound SNR.

To examine the resolution of the algorithm and the holographic experiment, a more complicated pattern based on the quantum walk experiment is also used, where adjacent pixels are associated with distinct intensity values along one direction. Both the simulation and the experimental result have shown a considerable coincidence with the desired pattern. For both test patterns, no speckle has been detected in the simulated data or in the measured data. Speckles act as scattering centres and hence have been considered as the biggest problem of GS-like algorithms. The SOMRAF algorithm is thus a powerful candidate for similar atom confinement experiments.

Blank Page.

Appendix

Note: in the context of this thesis including the appendix, the personal pronouns "we" refers to the reader(s) and me, the author of this thesis.

A.1 Wave propagation and Fresnel-Kirchhoff's integral

The derivations in this section are supported by the books [53, 54, 55].
The propagation of (optical) waves can be described by the Fresnel-Kirchhoff's integral which is based on the Huygens principle.
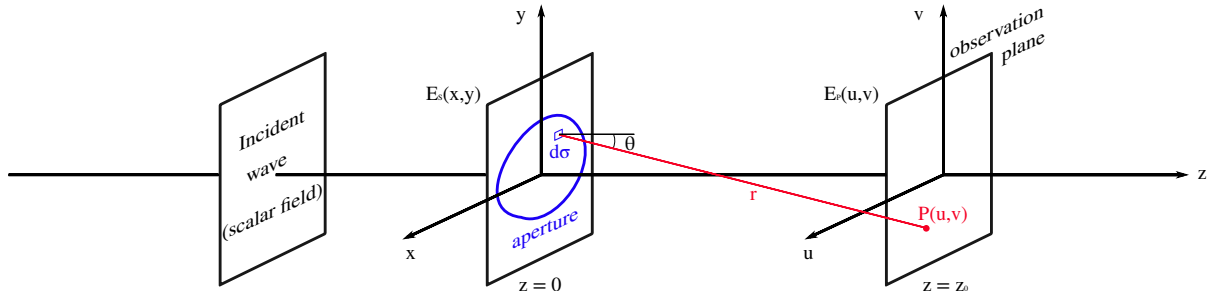
Fig. 7.1: Sketch for derivation of Fresnel-Kirchhoff's integral.

Let the incident wave be a scalar field and the resulting field at the aperture ($z = 0$) be denoted by $E_s(x, y) = A(x, y) \cdot e^{\phi(x,y)}$, with $A(x, y)$ the amplitude and $\phi(x, y)$ the phase of this field. According to the Huygens' principle, an infinitesimal area element $d\sigma = dx \cdot dy$ in the aperture plane emits secondary waves, which contributes

$$dE_P(u, v) = C \cdot \frac{E_S(x, y) \cdot d\sigma}{r} e^{ikr} \qquad (k = 2\pi/\lambda) \tag{7.1}$$

to the field at point $P(u, v)$ in the plane $z = z_0$. The factor $C = -\frac{i}{\lambda} \frac{1 + \cos\theta}{2}$ is called the proportionality factor and can be reduced to $-\frac{i}{\lambda}$ under paraxial approximation. Therefore, the entire field of the aperture σ yields the total field at point $P(u, v)$

$$E_P(u, v) = \int_\sigma C \cdot E_S(x, y) \cdot \frac{e^{ikr}}{r} d\sigma . \tag{7.2}$$

Equation 7.2 is called *Fresnel-Kirchhoff's diffraction integral.*

A.1.1 Fresnel approximation: near-field diffraction

After the Taylor expansion of distance r between the points in $d\sigma$ and the observation point $P(u, v)$

$$r = \sqrt{(x - u)^2 + (y - v)^2 + z_0^2} \approx z_0 \left(1 + \frac{(x - u)^2}{2z_0^2} + \frac{(y - v)^2}{2z_0^2} + ...\right) \tag{7.3}$$

and the approximation $r \approx z_0$ in the denominator of Equation 7.2, we reach the *Fresnel approximation*, namely the near-field diffraction:

$$E(u, v; z) = \frac{e^{ikz}}{i\lambda z} \int \int E_S(x, y) \cdot \exp\left[i\pi \frac{(x - u)^2 + (y - v)^2}{\lambda z}\right] dx\, dy. \tag{7.4}$$

This can be seen as a convolution relation, if we define a kernel $D_z(u, v) = \frac{1}{i\lambda z} \exp\left(i\pi \frac{u^2 + v^2}{\lambda z}\right)$. The Equation 7.4 is then re-written as

$$E_z(u, v) = \left[e^{ikz} E_S(u, v)\right] \circledast D_z(u, v), \tag{7.5}$$

where the first term in the RHS of the equation expresses the propagation of the wave on distance z and the kernel $D_z(u, v)$ here represents the complex amplitude of a spherical wave at centre O. This convolution relation expresses $E_z(u, v)$ as the sum of spherical waves produced by point-sources in the plane $z = 0$. The kernel $D_z(u, v)$ is the amplitude point spread function of the Fresnel diffraction and it's a normalized function:

$$\int \int D_z(u, v)\, du\, dv = 1. \tag{7.6}$$

A numerical simulation of Fresnel diffraction at the wavelength of 852 nm is shown in Figure 7.2.
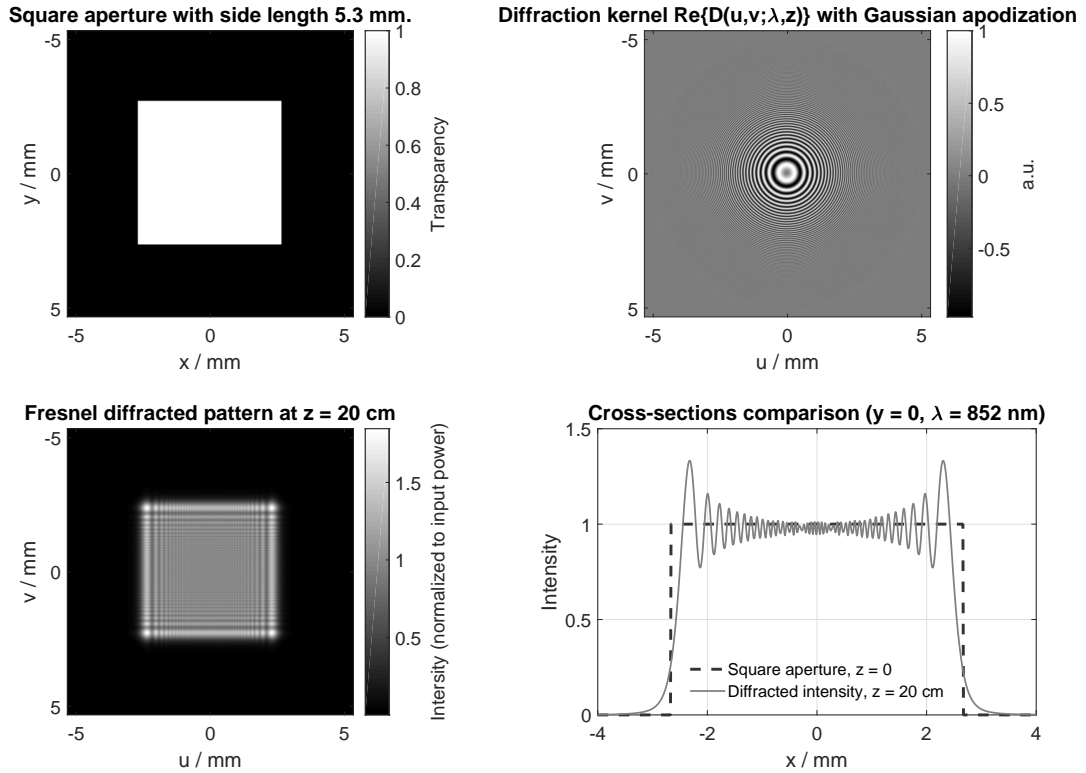
Fig. 7.2: Simulated Fresnel diffraction of a square aperture.

A.1.2 Fraunhofer approximation: far-field diffraction

Now let's rewrites Equation 7.4 again as

$$E_z(u, v) = \frac{e^{ikz}}{i\lambda z} \exp\left(i\pi \frac{u^2 + v^2}{\lambda z}\right) \int \int E_S(x, y) \cdot \exp\left[i\pi \frac{x^2 + y^2}{\lambda z} - i2\pi \frac{xu + yv}{\lambda z}\right] dx\, dy, \tag{7.7}$$

and introduce the Fresnel transform

$$E_z(u,v) = \frac{e^{ikz}}{i\lambda z} \exp\left(i\pi \frac{u^2 + v^2}{\lambda z}\right) \mathcal{F}\left[E_S(x,y) \cdot \exp\left(i\pi \frac{x^2 + y^2}{\lambda z}\right)\right], \tag{7.8}$$

where the symbol $\mathcal{F}$ denotes the Fourier transform with spatial frequencies $\frac{u}{\lambda z}$ and $\frac{v}{\lambda z}$. For $z \to \infty$ we reach the limit of the Fresnel diffraction - the *Fraunhofer diffraction.* The phase term $\exp\left(i\pi \frac{x^2+y^2}{\lambda z}\right)$ in Equation 7.8 tends towards 1. The complex field becomes

$$E_z(u,v) = \frac{e^{ikz}}{i\lambda z} \exp\left(i\pi \frac{u^2 + v^2}{\lambda z}\right) \hat{E}_S(\frac{u}{\lambda z}, \frac{v}{\lambda z}), \tag{7.9}$$

where we denote the Fourier transform of E_S by $\hat{E}_S$ for succinctness. Two numerical examples of Fraunhofer diffraction are shown in Figure 7.3. The far-field patterns of two rectangular apertures are simulated for a distance of 1.2 m.
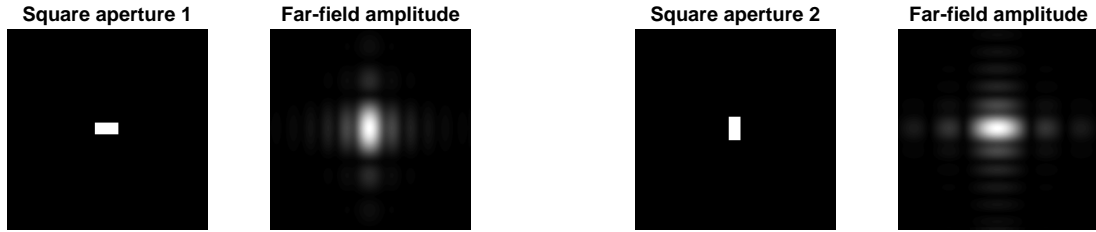
Fig. 7.3: Simulated Fraunhofer diffractions of two rectangular apertures.

A.1.3 Fourier transform property of a thin lens and the 2f-system

When working with laser which has a wavelength of several 100 nm, it's practical to use a converging lens with focal length f that allows us to observe the far-field diffraction at finite distance. To this, we shall introduce the *thin lens transmission function* [56] which acts as a phase transformation

$$t_f(x,y) = \exp\left(-i\pi \frac{x^2 + y^2}{\lambda f}\right) \tag{7.10}$$

to derive the property of a lens. f is positive for a converging lens and negative for a diverging one. Let's suppose that this lens is superimposed with the aperture at plane $z = 0$, so the total action on the incident wave can be expressed as the product $E_S(x,y) \cdot t_f(x,y)$. In the Fresnel transform in Equation 7.8, there is a particular distance $z = f$ for which the Fresnel diffraction takes the form of a Fourier transform

$$E_f(u,v) = \frac{e^{ikf}}{i\lambda f} \exp\left(i\pi \frac{u^2 + v^2}{\lambda f}\right) \hat{E}_S(\frac{u}{\lambda f}, \frac{v}{\lambda f}). \tag{7.11}$$

This is very similar to Equation 7.9. However, Equation 7.11 is only valid at $z = f$, whereas the Fraunhofer Equation 7.9 is valid at any large z.
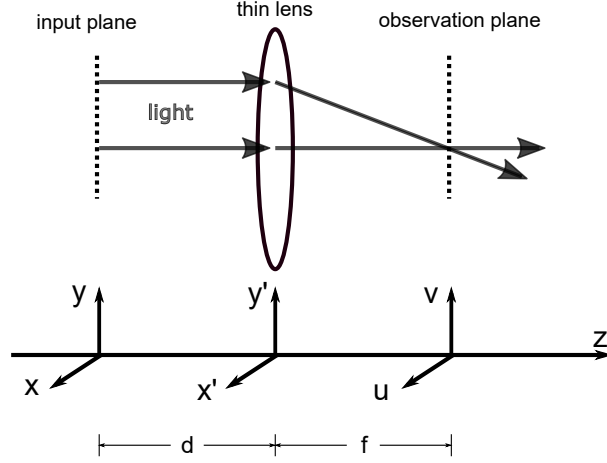
Fig. 7.4: Sketch for derivation of the Fourier transform property of thin lenses.

What would happen if the lens is not superimposed with the aperture? Figure 7.4 shows an additional configuration of interest. That is, the input plane lies at some distance d to the left plane of the lens and the observation plane is still the back focal plane of the lens. To deal with this scene, there is a two-step process.

- Step 1 (Fresnel diffraction): calculate the propagation of $E_S(x, y)$ from the (x, y) plane to the (x', y') plane, i.e. $E_d(x', y')$. For this, we apply the convolution theorem and rewrite Equation 7.5 as

$$\hat{E}_d(k_x, k_y) = e^{ikd} \, \hat{E}_S(k_x, k_y) \cdot \hat{D}_d(k_x, k_y), \tag{7.12}$$

with $k_x = x'/\lambda d$, $k_y = y'/\lambda d$. The transfer function $\hat{D}_d(k_x, k_y) = \exp\left[-i\pi\lambda d(k_x^2 + k_y^2)\right]^1$ is normalized and we have $\hat{D}_d(0,0) = 1$. Therefore, the Fourier transform of the field at the lens plane is expressed as

$$\hat{E}_d(k_x, k_y) = e^{ikd} \, \exp\left[-i\pi\lambda d(k_x^2 + k_y^2)\right] \hat{E}_S(k_x, k_y). \tag{7.13}$$

- Step 2 (thin lens transformation): calculate the transformation of the field from (x', y') plane to the (u, v) plane to obtain the final result $E_{d+f}(u, v)$. This can be simply done by inserting Equation 7.13 into Equation 7.11:

$$E_{d+f}(u, v) = \frac{1}{i\lambda f} \, e^{ikf} \, \exp\left(i\pi \frac{u^2 + v^2}{\lambda f}\right) e^{ikd} \exp\left[-i\pi\lambda d \frac{u^2 + v^2}{(\lambda f)^2}\right] \hat{E}_S(\frac{u}{\lambda f}, \frac{v}{\lambda f}) \tag{7.14}$$

$$= \frac{1}{i\lambda f} \, e^{ik(f+d)} \exp\left[i\pi \frac{u^2 + v^2}{\lambda f^2} \cdot (f - d)\right] \hat{E}_S(\frac{u}{\lambda f}, \frac{v}{\lambda f}). \tag{7.15}$$

The result is still proportional to the Fourier transform of the input field E_S. In the special case $d = f$, known as a 2f-system, the quadratic phase factor is equal to 1 and Equation 7.15 reduces to

$$E_{2f}(u, v) = \frac{1}{i\lambda f} \, e^{2ikf} \, \hat{E}_S(\frac{u}{\lambda f}, \frac{v}{\lambda f}), \tag{7.16}$$

having the exact Fourier transform relation up to a global phase factor, which is negligible.

---

[1] $\hat{D}_d(k_x) = \mathscr{F}[D_d(x')] = \sqrt{\frac{1}{i\lambda d}} \int_{-\infty}^{+\infty} \exp\left(i\pi \frac{x'^2}{\lambda d} - i2\pi k_x x'\right) \mathrm{d}x' = e^{-i\pi\lambda d k_x^2}$. Extending this to two dimensions yields $\hat{D}_d(k_x, k_y) = \exp\left[-i\pi\lambda d(k_x^2 + k_y^2)\right]$.

A.1.4 Fast Fourier transform (FFT) in MATLAB and Parseval's theorem

In the numerical simulations of the diffraction and phase retrieval in this work, it's crucial to preserve the norm of the matrix in order to produce correct results. The energy is conserved if the Parseval's theorem is obeyed. In case of an $N \times N$ matrix, the 2D fast Fourier transform `fft2` in MATLAB R2018a is defined as

$$\hat{f}[\mu\nu] = \texttt{fft2}(f[jk]) = \sum f[jk] \cdot \exp^{-2\pi i \frac{\mu j + \nu k}{N^2}} \,, \tag{7.17}$$

with μ, ν and j, k the matrix indices in the spatial plane and Fourier plane, respectively. In Equation 7.17, the transformation matrix is unitary. However, before verifying Parseval's theorem, let's define $\Delta x = 1$ pixel as the sampling interval, $K_s = 1/\Delta x$ as the sampling rate and $\Delta k = K_s/N$ as the frequency increment. Parseval's theorem required[1]

$$\sum ||f[jk]||^2 \cdot \Delta x^2 = \sum ||\hat{f}[\mu\nu]||^2 \cdot \Delta k^2 \,. \tag{7.18}$$

$||\cdot||$ denotes the norm. Therefore, $\Delta k = 1/N$ needs to be "merged" into $\hat{f}[\mu\nu]$, because the numerical process is operating in the unit of pixel. The 2D fast Fourier transform is thus rescaled as

$$\hat{f}[\mu\nu]_{\text{resc.}} = \frac{1}{N} \texttt{fft2}(f[jk]) \tag{7.19}$$

with the modulus scaling factor $1/N$. The definition of the inverse 2D fast Fourier transform `ifft2` in MATLAB is

$$f[jk] = \texttt{ifft2}\left(\hat{f}[\mu\nu]\right) = \frac{1}{N^2} \sum \hat{f}[\mu\nu] \cdot \exp^{2\pi i \frac{\mu j + \nu k}{N^2}} \,, \tag{7.20}$$

with an additional factor $1/N^2$ which is to be compensated by multiplying with N^2. So the inverse Fourier transform is

$$f[jk]_{\text{resc.}} = N \cdot \texttt{ifft2}\left(\hat{f}[\mu\nu]\right) \,. \tag{7.21}$$

after rescaling. In case of a general $N \times M$ matrix, the modulus rescaling factors for `fft2` and `ifft2` are $1/\sqrt{NM}$ and $\sqrt{NM}$, respectively.

A.2 Experimental data

A.2.1 Calculated holograms
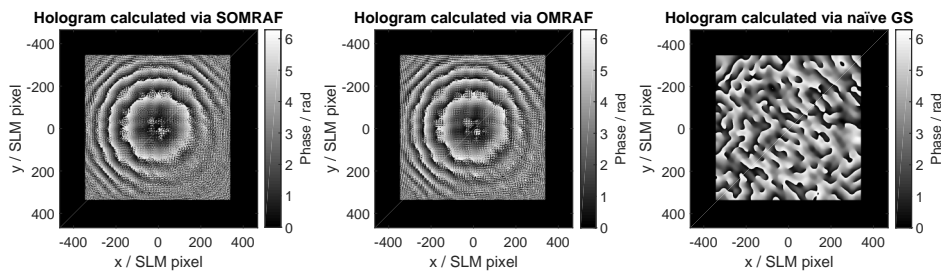
Fig. 7.5: Calculated 700×700 pixel holograms for pattern "plateau".

---

[1] Not $\sum ||f[jk]||^2 = \sum ||\hat{f}[\mu\nu]||^2$.
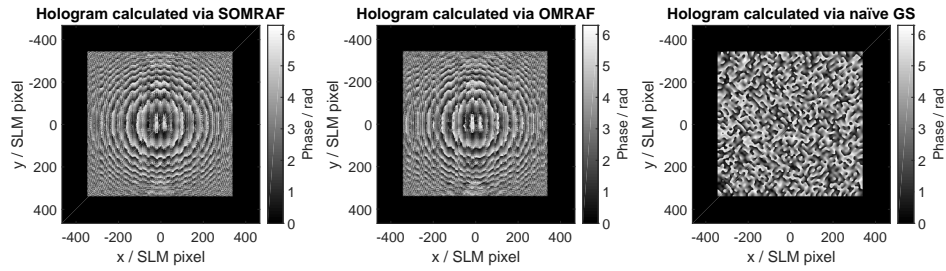
Fig. 7.6: Calculated 700×700 pixel holograms for pattern "ramps".

A.2.2 Single images of reconstructed patterns
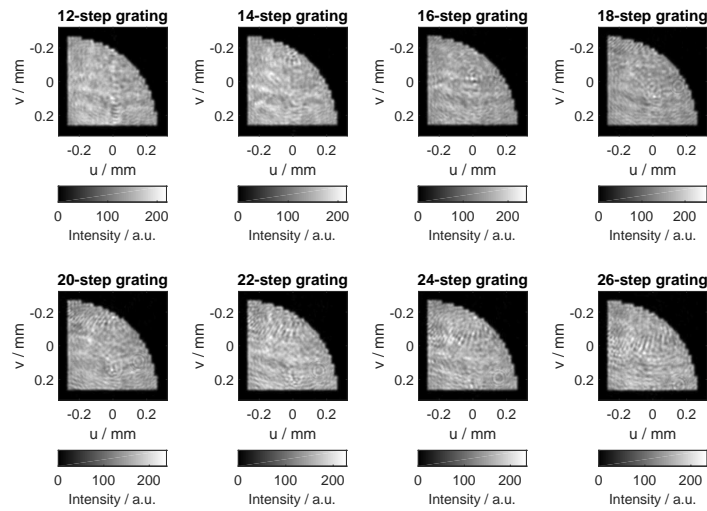
Fig. 7.7: Single images of pattern "plateau" measured at different diffracted positions (SOMRAF).
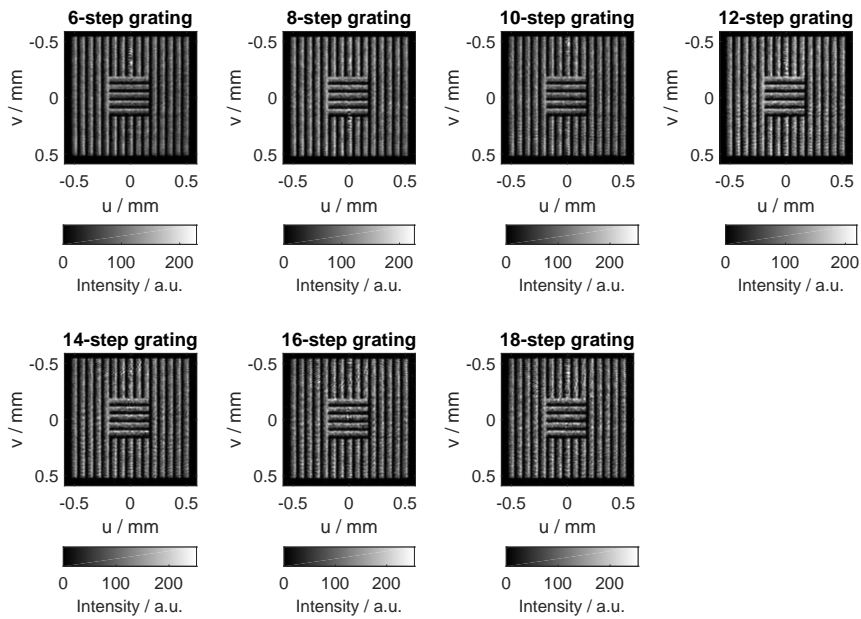
Fig. 7.8: Single images of pattern "ramps" measured at different diffracted positions (SOMRAF).

Bibliography

[1] Lord Rayleigh, *On the interference bands of approximately homogeneous light; in a letter to Prof. A. Michelson*, 1892, DOI: 10.1080/14786449208620352

[2] P.R.Millane, *Phase retrieval in crystallography and optics*, 1990, DOI: 10.1364/JOSAA.7.000394

[3] R.W.Harrison, *Phase problem in crystallography*, 1993, DOI: 10.1364/JOSAA.10.001046

[4] X-ray diffraction image of the double helix structure of the DNA molecule, taken 1952 by Raymond Gosling, commonly referred to as "Photo 51", during work by Rosalind Franklin on the structure of DNA. The photo can be seen in the link: `http://www-project.slac.stanford.edu/wis/images/photo_51.jpg`. Due to explicit statement of the use restriction, this photo is not used in this thesis.

[5] R.W.Gerchberg and W.O.Saxton, *A practical algorithm for the determination of the phase from image and diffraction plane pictures*, Cavendish Laboratory, Cambridge England 1972, Optik Vol.35 (No.2) 237-246 (1972)

[6] D.L.Misell, *A method for the solution of the phase problem in electron microscopy*, 1973, DOI: 10.1088/0022-3727/6/1/102

[7] J.Huang, H.Jin, Q.Ye and G.Meng, *Differential phase retrieval based on phase modulating for wavefront detection*, 2018, DOI: 10.1007/s00340-018-6928-7

[8] Y.Xu, Q.Ye and G.Meng, *Hybrid phase retrieval algorithm based on modified very fast simulated annealing*, 2018, DOI: 10.1017/S1759078718000971

[9] J.R.Fienup, *Phase retrieval algorithms: a comparison*, 1982, DOI: 10.1364/AO.21.002758

[10] T.Groh, S.Brakhane, W.Alt, D.Meschede, J.K.Asbóth and A.Alberti, *Robustness of topologically protected edge states in quantum walk experiments with neutral atoms*, 2016, DOI: 10.1103/PhysRevA.94.013620

[11] M.Sajid, J.K.Asbóth, D.Meschede, R.Werner and A.Alberti, *Creating Floquet Chern insulators with magnetic quantum walks*, 2018, arXiv:1808.08923v1

[12] D.Meschede, *Advanced Atomic, Molecular, and Optical Physics*, Lecture 12 (AC Stark effect), University Bonn, Winter 2015

[13] L.Allen, M.W.Beijersbergen, R.J.C.Spreeuw and J.P.Woerdman, *Orbital angular momentum of light and the transformation of Laguarre-Gaussian laser modes*, 1992, DOI: 10.1103/PhysRevA.45.8185

[14] D.Sayre, *The squaring method: A new method for phase determination*, 1952, DOI: 10.1107/S0365110X52000137

[15] H.Hauptman, *Phasing methods for protein crystallography*, 1997, DOI: 10.1016/S0959-440X(97)80077-2

[16] A.Levi and H.Stark, *Image restoration by the method of generalized projections with application to restoration from magnitude*, 1984, DOI: 10.1364/JOSAA.1.000932

[17] H.H.Bauschke, P.L.Combettes and D.R.Luke, *Phase retrieval, error reduction algorithm, and Fienup variants: a view from convex optimization*, 2002, DOI: 10.1364/JOSAA.19.001334

[18] E.Osherovich, *Numerical methods for phase retrieval*, PhD Thesis, Israel Institute of Technology, 2011, arXiv:1203.4756v1

[19] M.Hayes, *The reconstruction of a multidimensional sequence from the phase or magnitude of its Fourier transform*, 1982, DOI: 10.1109/TASSP.1982.1163863

[20] F.Wyrowski and O.Bryngdahl, *Iterative Fourier-transform algorithm applied to computer holography*, 1988, DOI: 10.1364/JOSAA.5.001058

[21] S.Boyd and L.Vandenberghe, *Convex Optimization*, Cambridge University Press, ISBN 0 521 83378 7

[22] J.F.Nye, M.V.Berry and F.C.Frank, *Dislocations in wave trains*, 1974, DOI: 10.1098/rspa.1974.0012

[23] M.Pasienski and B.DeMarco, *A High-Accuracy Algorithm for Designing Arbitrary Holographic Atom Traps*, 2008, DOI: 10.1364/OE.16.002176

[24] A.L.Gaunt and Z.Hadzibabic, *Robust Digital Holography For Ultracold Atom Trapping*, 2012, DOI: 10.1038/srep00721

[25] H.Wang et al., *A hybrid Gerchberg–Saxton-like algorithm for DOE and CGH calculation*, 2016, DOI: 10.1016/j.optlaseng.2016.04.005

[26] G.Situ and H.Wang, *Phase problems in optical imaging*, 2017, DOI: 10.1631/FITEE.1700298

[27] W.Hsu and S.Lin, *Iterative pixelwise approach applied to computer-generated holograms and diffractive optical elements*, 2018, DOI: 10.1364/AO.57.00A189

[28] V.Soifer, V.Kotlyar and L.Doskolovich, *Iterative Methods for Diffractive Optical Elements Computation*, 1997, Taylor & Francis, Bristol, PA, ISBN 978-0-7484-0634-0

[29] F.Kleißler, *Assembly and Characterization of a High Numerical Aperture Microscope for Single Atoms*,Master Thesis, University Bonn, 2014

[30] W.Zhou, *Analyse der Punktspreizfunktion des Abbildungssystems vom DQSIM-Experiment anhand der Fluoreszenzaufnahmen*, Bachelor Thesis, University Bonn, 2016

[31] E.Candès, T.Strohmer and V.Voroninski, *PhaseLift: Exact and Stable Signal Recovery from Magnitude Measurements via Convex Programming*, 2011, arXiv:1109.4499v1

[32] I.Waldspurger, A.d'Aspremont and S.Mallat, *Phase Recovery, MaxCut and Complex Semidefinite Programming*, 2013, arXiv:1206.0102v3

[33] E.Candès, X.Li and M.Soltanolkotabi, *Phase Retrieval via Wirtinger Flow: Theory and Algorithms*, 2015, arXiv:1407.1065v3

[34] V.Elser, T.Lan and T.Bendory, *Benchmark problems for phase retrieval*, 2018, arXiv:1706.00399v3

[35] A.Jesacher, *Applications of spatial light modulators for optical trapping and image processing*, PhD Thesis, Leopold-Franzens University Innsbruck, 2007

[36] C.Lingel, T.Haist and W.Osten, *Optimizing the diffraction efficiency of SLM-based holography with respect to the fringing field effect*, 2013, DOI: 10.1364/AO.52.006877

[37] H.Dammann, *Spectral characteristic of stepped-phase gratings*, Optik **53**, 409-417 (1979)

[38] A.Knieps, *A Spatial Light Modulator for Steering Quantum Walks with Single-Site Precision*, Master Thesis, University Bonn, 2016

[39] J.Schmitz, *Aufbau und Betrieb eines räumlichen Lichtmodulators*, Bachelor Thesis, University Bonn, 2015

[40] M.Kujawinska, R.Porras-Aguilar, and W.Zaperty, *LCoS spatial light modulators as active phase elements of full-field measurement systems and sensors*, DOI: 10.2478/v10178-012-0038-3

[41] A.Jesacher, A.Schwaighofer, S. Fürhapter, C.Maurer, S.Bernet and M.Ritsch-Marte, *Wavefront correction of spatial light modulators using an optical vortex image*, 2007, DOI: 10.1364/OE.15.005801

[42] M.Persson, D.Engström and M.Goksör, *Reducing the effect of pixel crosstalk in phase only spatial light modulators*, 2012, DOI: 10.1364/OE.20.022334

[43] A.E.M.Browar, M.Shusteff, R.M.Panas, J.D.Ellis and C.M.Spadaccini, *Overview and Comparison of Spatial Light Modulator Calibration Methods*, 31st ASPE Annual Meeting (2016), Report number: LLNL-CONF-686901

[44] C.Lingel, C.Thiel, T.Haist and W.Osten, *Fringing Field Effect and the measurement of the subpixel Jones matrices of an LCD*, DGaO Proceedings 2012, ISSN:1614-8436, urn:nbn:de:0287-2012-A037-6

[45] B.Apter, U.Efron and E.Bahat-Treidel, *On the fringing-field effect in liquid-crystal beam-steering devices*, 2004, DOI: 10.1364/AO.43.000011

[46] M.Persson, *Advances in Holographic Optical Trapping*, PhD Thesis, University of Gothenburg, 2013

[47] J.L.Martinez Fuentes, E.J.Fernandez, P.M.Prieto and P.Artal, *Interferometric method for phase calibration in liquid crystal spatial light modulators using a self-generated diffraction-grating*, 2016, DOI: 10.1364/OE.24.014159

[48] M.B.Roopashree, A.Vyas, R.K.Banyal and B.R.Prasad, *Phase characteristics of reflecting and transmitting type twisted nematic spatial light modulators*, arXiv:0911.0817

[49] D.Engström, M.Persson, J.Bengtsson and M.Goksör, *Calibration of spatial light modulators suffering from spatially varying phase response*, 2013, DOI: 10.1364/OE.21.016086

[50] Z.Zhang, H.Yang, B.Robertson, M.Redmond, M.Pivnenko, N.Collings, W.A.Crossland and D.Chu, *Diffraction based phase compensation method for phase-only liquid crystal on silicon devices in operation*, 2012, DOI: 10.1364/AO.51.003837

[51] D.C.Ghiglia and L.A.Romero, *Robust two-dimensional weighted and unweighted phase unwrapping that uses fast transforms and iterative methods*, 1994, DOI: 10.1364/JOSAA.11.000107. The MATLAB code of the unwrapping process is written by M.F.Kasim from University of Oxford 2016.

[52] The goodnesses of fit of MATLAB built-in functions are automatically calculated. Please check `https://www.mathworks.com/help/matlab/data_analysis/linear-regression.html#f1-15010` for the definition of R^2.

[53] S.J.Orfanidis, *Electromagnetic Waves and Antennas*, Chapter 20, 2016. The book can be freely downloaded from `https://www.ece.rutgers.edu/~orfanidi/ewa/ewa-1up.pdf`

[54] D.Meschede, *Optik, Licht und Laser*, Kap. 2, 1999 B.G.Teubner Stuttgart·Leipzig

[55] W.Demtröder, *Experimentalphysik 2: Elektrizität und Optik*, Kap. 10, 6. Auflage Springer Spektrum

[56] E.Candès, *Applied Fourier Analysis and Elements of Modern Signal Processing*, Lecture 17, Stanford University, Winter 2016

Declaration of images and tools

All of the vectorial illustrations presented in this thesis are drawn by myself using the software Inkscape, except for the explaining figures 2.1 and 3.8, which are kindly provided by my former colleague Dr. Muhammad Sajid and my team leader Dr. Andrea Alberti.

The pixel-wise cosine fitting in the phase-shifting interferometry (PSI), a pre-selection of various 2D unwrapping methods, the framework of coordinate transformation between CCD pixel and SLM pixel have been investigated and successfully established by my colleague Richard Winkelmann with the software MATLAB during his preparatory investigation of the SLM. I have further refined the MATLAB routine of PSI for the purpose of wavefront measurement. Other algorithmic simulations as well as the numerical analysis in both spatial and Fourier domains are done by myself during this work and in a previous work [30] with the software MATLAB.

Blank Page.

Acknowledgements

Characterization of the LCoS SLM-100 of Santec

Investigation on the cross-talk effect

Anomalous phenomenon of the horizontal diffraction direction with a period of two pixels

Weiqi Zhou

Bonn, Oct 8th 2018

Abstract

In this report, we summarize the qualitative observation (spatial domain) and the quantitative investigation (Fourier domain) on the pixel cross-talk effect of the LCoS SLM-100 from Santec in both vertical and horizontal directions. In these tests, the horizontal diffraction direction has shown an anomalous phenomenon where the diffraction efficiency in the horizontal direction is much lower than our theoretical expectation and, most importantly, lower than the corresponding diffraction efficiency in the vertical direction. Experimental methods and setups as well as measured physical quantities and the results will be demonstrated with figures in this report.

Contents

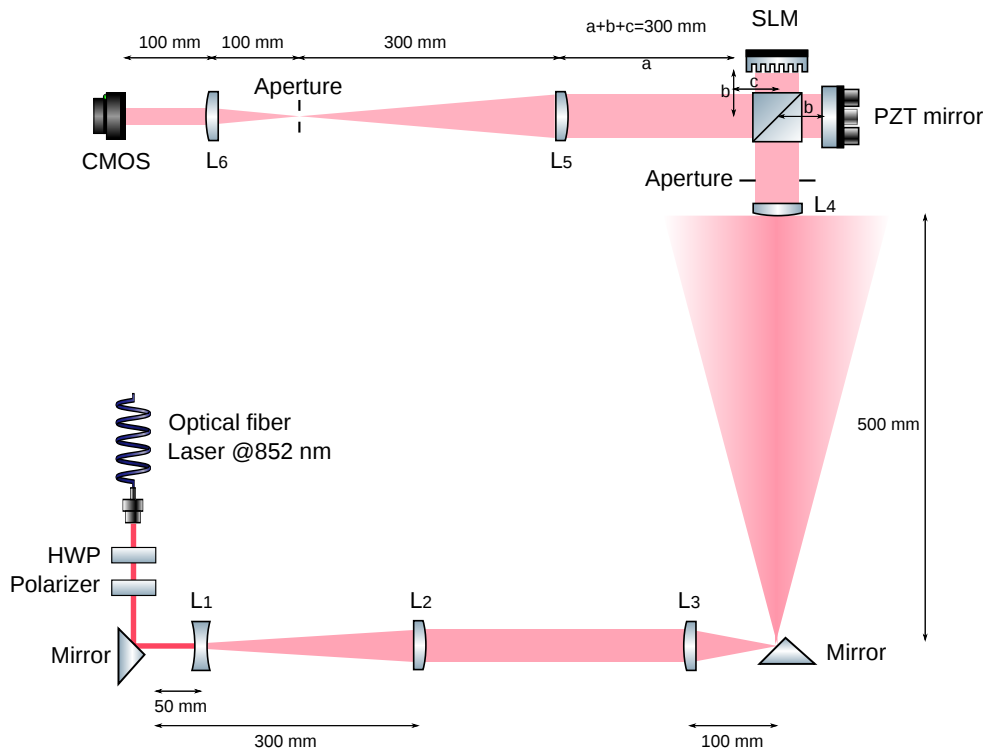# 1 Direct observation in the spatial domain

Figure 1: Setup: phase-shifting interferometric measurement of the SLM curvature. An 852 nm laser beam coming out from an optical fiber is first collimated and its polarization is optimized by rotating the half-wave plate and the polarizer after the fiber. To obtain a flat incident wavefront at the SLM stage, two set of amplification telescopes (L_1 and L_1, L_3 and L_4) are inserted between the laser source and the interferometer. The interferograms are than projected through a reduction telescope (L_5 and L_6) onto the camera chip. The piezo reference mirror, the SLM and the CMOS camera are controlled via computer softwares.

Before the observation of the SLM pixel cross-talk effect, we measured the physical curvature of the SLM layers using phase-shifting interferometry [1] (PSI, configuration: Tywman-Green interferometer). The setup is shown and explained in Figure 1. We also carried out a pixel-wise gamma test of the phase response using the same method in case of 852 nm, the wavelength required in our experiment. The PV value of the measured SLM curvature read $2.14\,\lambda$ and after compensation the residual RMS measured $\lambda/78$. The result of the compensation is shown in Figure 2.
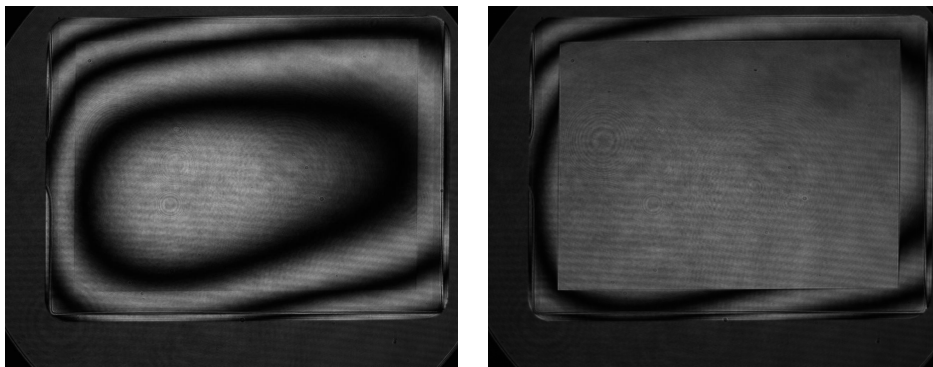

Figure 2: Interferograms of the Twyman-Green interferometer before (left) and after (right) the SLM curvature correction

Then we replaced the reduction telescope (L$_5$ and L$_6$) by an amplifying one (80 mm - 1000 mm , i.e. amplification of 12.5 times) in order to observe the pixel cross-talk effect spatially. Our CMOS camera has a pixel size of 5.2 μm and thus every SLM pixel was projected onto 25 camera pixels theoretically. This measurement was carried out separately in the vertical and horizontal directions. We applied different phase patterns onto the SLM such as a binary barrier, a simple phase step and linear ramps along one direction. Then we measured the phase via PSI again and took the average values along the corresponding direction to obtain the 1D phase profiles. In these measurements, the imaging system had slight astigmatism and we have adjusted the distance accordingly for each direction to ensure sharp images.

The vertical direction

A one-pixel-barrier of $1.5\,\pi$, a phase step of the same height and four 8-pixel linear ramps (blue curves in the three plots in Figure 3) as well as their complementaries (magenta curves) were measured in the vertical direction.
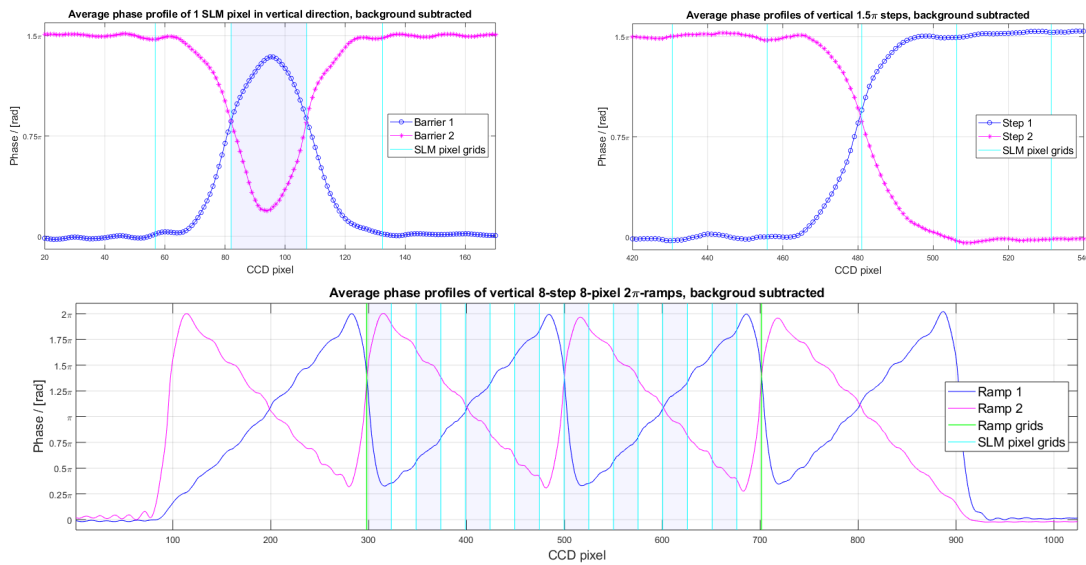

Figure 3: Upper row left: one-pixel-barriers of $1.5\,\pi$, the SLM pixel with distinct phase value as the other pixels is high-lighted; upper row right: steps of $1.5\,\pi$; lower row: four 8-pixel $2\,\pi$ ramps, 16 SLM pixels are highlighted in the central two ramps. The phase patterns and their complementaries are plotted in blue curves and magenta curves, respectively. The results agree with our expectation of the cross-talk effect qualitatively.

The observation in the vertical direction agrees with our expectation of the cross-talk behaviour, when significantly different phase/voltage values are applied onto the adjacent pixels. However, the measurement of linear ramps in the horizontal direction came out to be chaotic, which brought us to investigate the horizontal cross-talk effect in concrete pixel coordinates.

The horizontal direction

We first observed the SLM surface by the Thorlabs camera through the telescope while applying different phase patterns onto it. This direct observation has shown a two-pixel periodicity of some anomalous phase response between adjacent pixels in case of significantly different phases. For $N \in [1, 1440/2]$, if the involved two pixels were pixel No. $2N-1$ and pixel No. $2N$, the phenomenon did not occur and it looked like the vertical direction; but if the involved two pixels were pixel No. $2N$ and pixel No. $2N+1$, this phenomenon arose. Let's look into this problem in details, see Figure 4. If a

single binary phase barrier of even number width is applied to the SLM, both edges behave the same way: both anormal (the first plot of Figure 4) or both normal if the barrier is translated by one pixel (the second plot of Figure 4); if the barrier width is odd, both edges behave contrarily: one is anormal while the other is normal, and vice versa if the entire barrier is translated by one pixel (the third and the fouth plots of Figure 4).
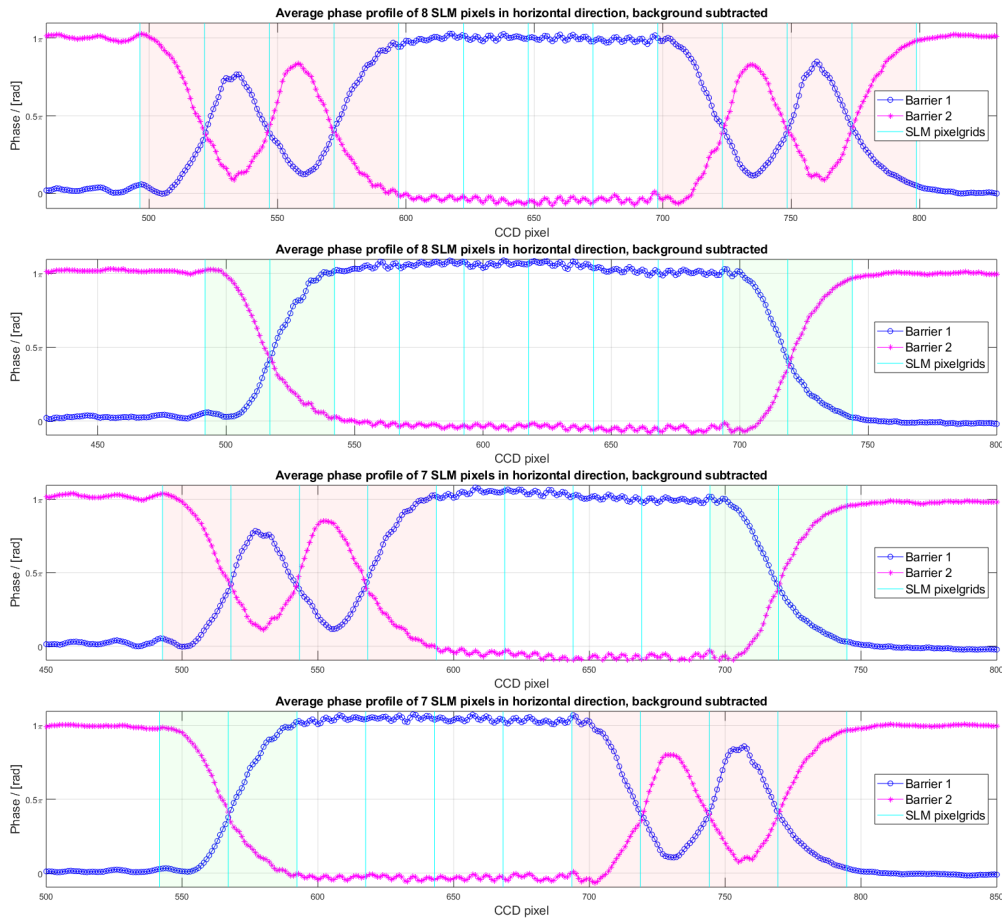

Figure 4: The anomalous phase behaviour of the horizontal direction, which seems to be 2-pixel periodic. If the cross-talk behaves normally, it affects the two involved adjacent pixels (green areas), otherwise four pixels (red areas).
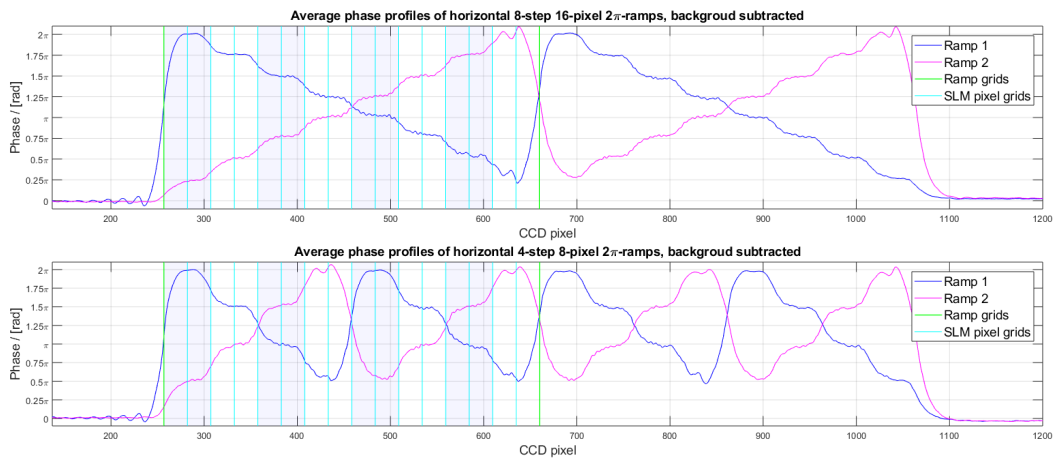

Figure 5: The horizontal direction works only in superpixel modus if the pixels are binned correctly and at the cost of losing half of the resolution. 16 SLM pixels are highlighted in the left half of the patterns. Every two adjacent pixels make a superpixel.

3

Binning the adjacent pixels at the problem positions to avoid phase difference there could help to avoid anormal phase behaviour, for example we were able to measure linear ramps without having chaotic problem any more (Figure 5), but we lost half of the resolution in this direction.

2 Indirect investigation in the Fourier domain

After characterization of the SLM flatness and gamma curve, we created some simple Faunhofer diffraction patterns in the Fourier plane of a 2f-correlator. Figure 6 shows the first-order diffracted patterns of OAM beams before and after our SLM flatness compensation while applying a vertical blazed grating.

Far-field images of OAM beams (LG$_{00}$, LG$_{01}$, LG$_{02}$) without SLM flatness correction
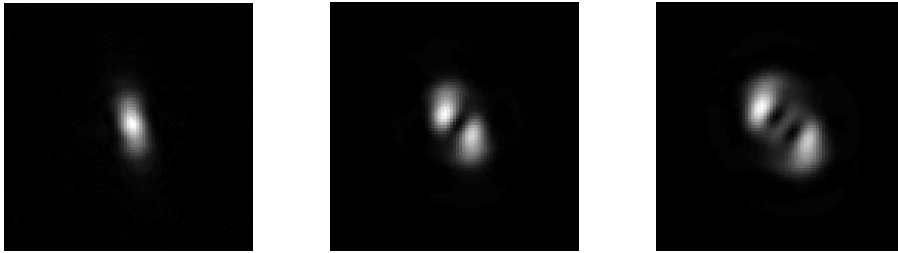
Far-field images of OAM beams (LG$_{00}$, LG$_{01}$, LG$_{02}$) after SLM flatness correction
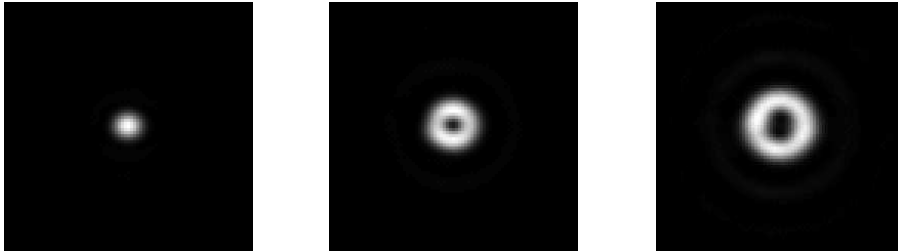

Figure 6: OAM beams before and after SLM flatness error correction.

In the horizontal diffraction direction we also obtained the patterns with similar quality, but the brightness was much smaller, the reason for which was that part of the incident light has been diffracted into other orders due to the anormal phase response discussed above. Thus we measured the ratio between the intensity of the first-order pattern and the intensity of the zero-order pattern when no grating is applied, and defined this ratio as the diffraction efficiency (DE) in this measurement. The DE is measured for both directions for blazed gratings of varying periodic lengths and the results are shown in Figure 7.

The theoretical curve is given by [2, 3], under the assumption of an ideal SLM with 100% fill factor and without pixel cross-talk effect. Due to a finite fill factor and the existing cross-talk effect of a conventional LC SLM, the measured curve will lie under the theoretical one. It's obvious that

the horizontal direction is suffering from the anormal phase behaviour and the its DE curve (green) significantly deviates from the vertical one (red). Binning the adjacent pixels to create a superpixel enhances the DE (blue) but loses half of the resolution. In a different attempt to correct for the problem, we addressing the pixel pairs with anomalous behaviours, and lift the lower phase by 2π when the phase difference exceed 60% of 2π preserves the resolution but the enhanced DE (magenta) still lies far below the vertical curve. The distortion of the diffracted pattern increases with the steepness of the grating, where the situation in the horizontal direction is again worse than in the vertical direction, compare the first column and the second column of Figure 8.
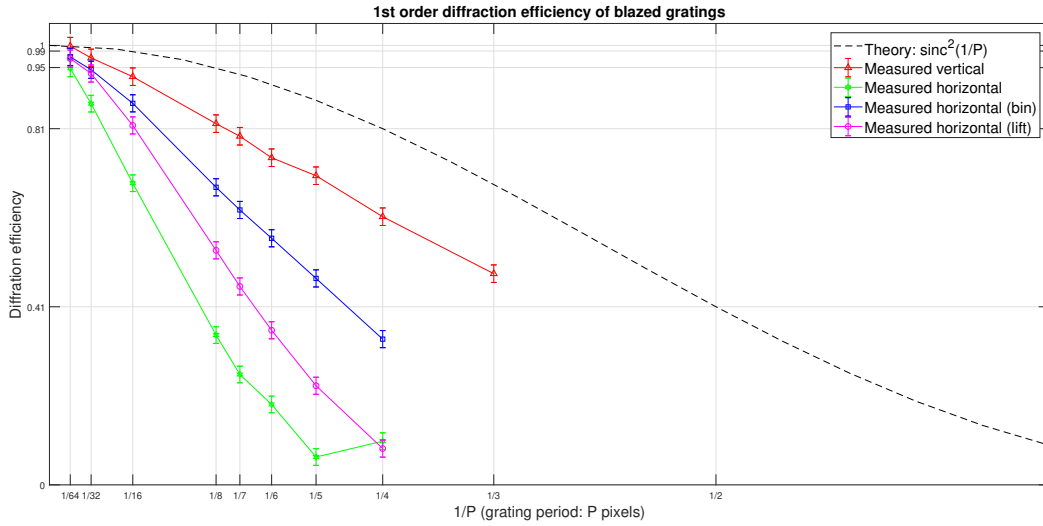

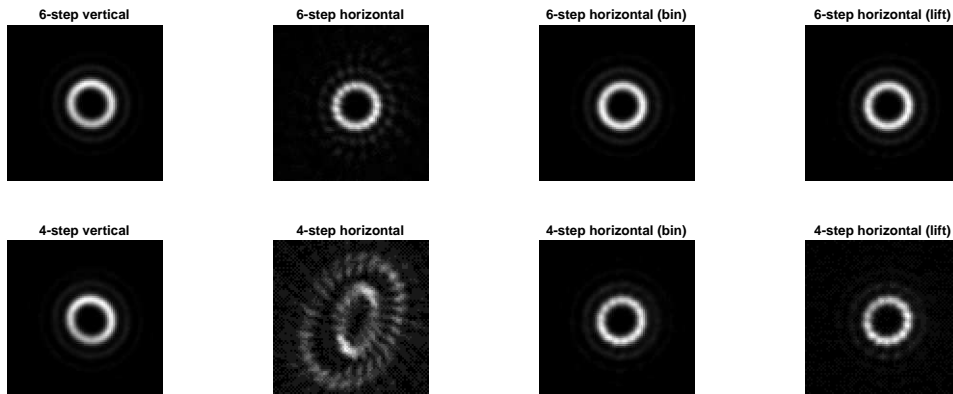Figure 7: First-order diffraction efficiencies of blazed gratings.

Figure 8: First-order diffraction patterns of LG_{07}-mode for 6-step and 4-step blazed gratings. First column: vertical gratings; second column: horizontal gratings; third column: horizontal gratings in bin modus; fouth column: horizontal gratings in lift modus. The distortion of the doughnuts in case of steep ramps in the horizontal direction is larger than in the other direction. The two mentioned DE enhancing methods could also correct the distortion.

References

[1] A.Jesacher, Applications of spatial light modulators for optical trapping and image processing, PhD Thesis, Leopold-Franzens University, Innsbruck 2007

[2] C.Lingel, T.Haist, and W.Osten, Optimizing the diffraction efficiency of SLM-based holography with respect to the fringing field effect, OSA 2013, DOI:10.1364/AO.52.006877

[3] H.Dammann, Spectral characteristic of stepped-phase gratings, Optik **53**, 409-417 (1979)